Flat slab-induced hydration weakening and destruction of the North China Craton

Jyotirmoy Paul[1], Arne Spang[1], and Andrea Piccolo[2]

[1]University of Bayreuth
[2]Mainz Institute of Microtechnology

April 12, 2024

Abstract

In this study, we develop two dimensional (2-D) box models to identify the most viable reasons for the destruction of the North China Craton (NCC). We examine the role of flat slab-induced hydration, high-density lower crust, and weak mid-lithospheric discontinuity in our models. Results indicate that flat slab-induced hydration weakening of the eastern part of the NCC can lead to rapid craton destruction if hydration weakening rates are sufficiently fast. This accelerated hydration rate may be attributed to the extensive carbonatite magmatism within the eastern part of the NCC, facilitating a faster pathway for water diffusion throughout the craton. Craton destruction is contingent upon the craton's density exceeding the surrounding mantle density, and its viscosity decreasing below 1022 Pa s. We observe that the presence of a dense lower crust or a weak mid-lithospheric discontinuity fail to destroy the NCC unless it is weakened.

Flat slab-induced hydration weakening and destruction of the North China Craton

Jyotirmoy Paul, Arne Spang, Andrea Piccolo

Bayerisches Geoinstitut, Universität Bayreuth, 95447 Bayreuth, Germany

Key Points:

- Investigation of North China Craton (NCC) destruction with thermomechanical numerical models.
- Flat slab-induced hydration can sufficiently weaken eastern part of the North China Craton (NCC).
- Craton is destroyed if its density is higher than the underlying mantle and its viscosity is lower than 10^{22} Pa s.

Corresponding author: Jyotirmoy Paul, jyotirmoy.paul@uni-bayreuth.de

Abstract

In this study, we develop two dimensional (2-D) box models to identify the most viable reasons for the destruction of the North China Craton (NCC). We examine the role of flat slab-induced hydration, high-density lower crust, and weak mid-lithospheric discontinuity in our models. Results indicate that flat slab-induced hydration weakening of the eastern part of the NCC can lead to rapid craton destruction if hydration weakening rates are sufficiently fast. This accelerated hydration rate may be attributed to the extensive carbonatite magmatism within the eastern part of the NCC, facilitating a faster pathway for water diffusion throughout the craton. Craton destruction is contingent upon the craton's density exceeding the surrounding mantle density, and its viscosity decreasing below 10^{22} Pa s. We observe that the presence of a dense lower crust or a weak mid-lithospheric discontinuity fail to destroy the NCC unless it is weakened.

Plain Language Summary

Cratons, constituting the oldest part of Earth's lithosphere, often exceed 3 billion years in age. Despite continuous recycling due to plate-tectonics on Earth, cratons maintain tectonic stability owing to their viscosity, density, and thickness. Nevertheless, certain geological activities can lead to the partial or complete destruction of cratons. A prime example is the North China Craton (NCC), where the eastern half has undergone extensive thinning. The mechanism behind the NCC's destruction has been a subject of debate for over the last two decades. In this study, we develop numerical models to investigate the most viable geodynamic scenario for the destruction of the NCC. We find hydration weakening, induced by fluids from the subducting slab, is the key control for craton destuction. Geological evidence indicates the flattening of the subducting slab during the Jurassic period. The presence of a flat slab likely facilitated partial hydration of the eastern half of the craton, while the western half remained intact. Subsequently, the weakened eastern segment could have been destroyed due to underlying mantle flow if the craton possessed a density exceeding underlying mantle and a viscosity lower than 10^{22} Pa s.

1 Introduction

Destruction of the North China Craton (NCC) (F.-Y. Wu et al., 2019; J. T.-J. Wu et al., 2022; Y.-F. Zheng et al., 2013; Zhu et al., 2012) challenges the notion of immortal cratons in geological history. Geophysical evidence, including the global litihospheric thickness model (Conrad & Lithgow-Bertelloni, 2006) (Fig. 1 A), slow seismic velocity anomalies in tomography models (Ritsema et al., 2004)(Fig. 1 A), and geochemical observations from xenolith studies (Menzies et al., 1993; Xu, 2001; Yang et al., 2008; J. Zheng et al., 2005; Y. Zheng et al., 2018; Zhu et al., 2012), firmly establish that the eastern part of the North China Craton is thinner than its western counterpart. Prior ∼200 Ma (early Jurassic period), the entire craton existed with a passive margin boundary and a normal cratonic thickness of approximately 200 km (Z. Wang & Kusky, 2019, c.f.). After 200 Ma, the onset of paleo-Pacific subduction along the eastern margin of the NCC reactivated the craton margin (Tang et al., 2018). In the early Cretaceous period (∼ 130 - 100 Ma), the eastern part of the craton thickness was reduced to around 100 km (Zhu et al., 2012; F.-Y. Wu et al., 2019; J. T.-J. Wu et al., 2022; J. Zheng et al., 2005; Y. Zheng et al., 2018; J. Liu et al., 2019). Although there is consensus regarding the extensive thinning of the NCC, the mechanism behind it remains a subject of debate.

Previous studies proposed a range of possible mechanisms that could destroy the eastern part of the NCC. The onset of paleo-Pacific subduction at the eastern margin of the NCC has been considered as one of the most likely reasons for craton destruction (Xu, 2001; J. Zheng et al., 2005). The nature of the subduction zone remained disputed for a long time until recently, when several studies proposed the existence of a flat slab in this region. F.-Y. Wu et al. (2019) showed an age reversal of igneous rocks along an east-west transect from the paleo-subduction zone to the middle of the craton (Fig. 1 B). Many of these igneous activities are associated with carbonatite intrusions, particularly from the eastern part of the NCC (Chen et al., 2016, 2017; X. Wang et al., 2022). During the late Triassic and Jurassic periods, magmatic activities moved towards the continental interior, and in the Cretaceous period, magmatism migrated towards the sea (Fig. 1 C). This reversal is interpreted as the onset of westward flat subduction of the Paleo-Pacific slab around 200 Ma, followed by slab rollback at approximately 160 - 140 Ma (Y. Zheng et al., 2018; J. Liu et al., 2019; F.-Y. Wu et al., 2019; J. T.-J. Wu et al., 2022) (Fig. 1 C). The presence of a flat slab could have hydrated the eastern part of the craton (Fig. 1 C, hatched region) (F.-Y. Wu et al., 2019; J. T.-J. Wu et al., 2022; Y. Zheng et al., 2018), while the western block remained dry (Xia, Hao, et al., 2013). Xia, Liu, et al. (2013) studied the clinopyroxene samples of early Cretaceous basalts from the Feixian region (Fig. 1 A) and found high water content within them. They estimated that such high water content in clinopyroxene samples is possible only if the cratonic mantle contained at least 1000 ppm water before $\sim$ 120 Ma. Such high water content can change the 'dry' olivine rheology to 'wet' olivine (Hirth & Kohlstedt, 2003; Mei & Kohlstedt, 2000; Xia, Liu, et al., 2013), significantly reducing the overall viscosity of the lithospheric mantle. Weaker cratons potentially form lithospheric drips depending on their 'available buoyancy' (Conrad & Molnar, 1999), and those drips are removed gradually. Y. Zheng et al. (2018) attributed the NCC destruction to such a bottom-to-top process.

There are other mechanisms that could also have destroyed the NCC. Due to high pressure and temperature, dense eclogites are formed within the thick lower crust. This dense layer initiates a gravitational instability which can delaminate the crust, and eventually destroy the cratonic lithosphere by a process called foundering (Gao et al., 2004). Other studies have suggested the presence of a weak mid-lithospheric discontinuity (MLD) as another potential reason for craton destruction (Liao & Gerya, 2014; L. Liu et al., 2019; Shi et al., 2020; Z. Wang & Kusky, 2019). Unlike the slab-induced process, these two destruction mechanisms are top-to-bottom processes, where craton destruction initiates at the top margin (Y. Zheng et al., 2018).

In this study, we use thermomechanical numerical models to investigate the evolution and destruction of the North China Craton. We investigate several scenarios to test their mechanical and geodynamical viability. Though our primary focus is to understand flat slab-induced destruction, we also examine cases in the presence of a dense lower crustal layer and a weak mid-lithospheric discontinuity. We explore different parameters, including density, viscosity, and the rate of hydration to support our arguments. We calibrate the timing of destruction with geologically observed data.

2 Geodynamic model

We develop time-dependent geodynamic models, using the thermomechanical finite differences code LaMEM (Kaus et al., 2016, details in supplementary text S1) which is routinely used to model subduction dynamics (Pusok & Stegman, 2020; Riel et al., 2023). Our 2D model domain consists of a Cartesian box of 4000$\times$1000 km (Fig. 2A) and is built with geomIO (Bauville & Baumann, 2019; Spang, Baumann, & Kaus, 2022). The continental block comprises a 40 km thick continental crust, followed by a thick continental lithosphere down to 100 km and a cratonic lithosphere root extending to a depth of 200 km, with a width of 2000 km (Fig. 2 A). Below the continental lithosphere, the upper mantle extends to 660 km depth, and the lower mantle to 1000 km. Each layer is distinguished by a specific rheology given in supplementary table S1 (Hirth & Kohlstedt, 2003; Tirel et al., 2008). To simulate the paleo-Pacific subduction zone, we place a flat slab along the eastern margin of the craton following the approach of F.-Y. Wu et al. (2019) (Figs. 1 C, 2 A). The flat slab extends to the middle of the craton's width,

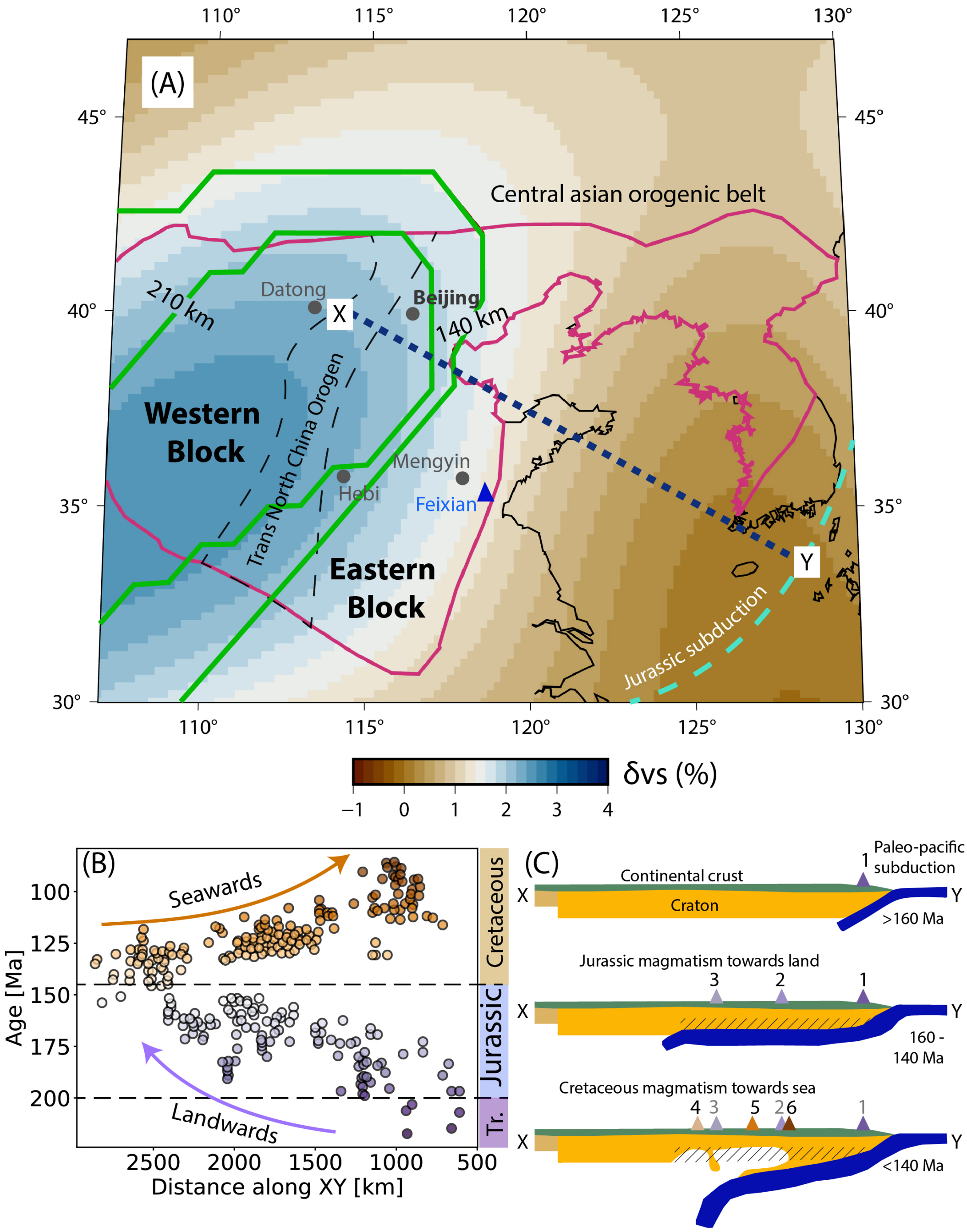

Figure 1. (A) Location of the North China Craton (NCC) marked by pink boundary. The western and eastern blocks of the NCC are separated by the trans North China orogen. The background colors in the Figure represent the shear wave velocity anomaly from the S20RTS tomography model (Ritsema et al., 2004), and the green lines are the contours of lithosphere thickness of 210 and 140 km, obtained from the global lithosphere thickness model of Conrad and Lithgow-Bertelloni (2006). Present-day coastlines are in black. Several igneous rocks are dated along the X-Y transect (F.-Y. Wu et al., 2019; J. T.-J. Wu et al., 2022). (B) Age distribution of igneous rocks along X-Y transect extracted and complied from (Z. Wang & Kusky, 2019; J. T.-J. Wu et al., 2022). (C) Schematic diagram of destruction of North China Craton modified after J. Liu et al. (2019); F.-Y. Wu et al. (2019); J. T.-J. Wu et al. (2022). 1-6 represent progression of magmatic activity with time.

hypothetically dividing it into eastern and western part. The mantle flow dynamics are driven by the density anomaly of the slab and an additional inflow of 1-2 $\mathrm{cm\,yr^{-1}}$ from the eastern margin of our model. Additionally, a temperature difference of 1600 K between the top and the bottom of the model also contributes to the vigour of mantle flow. The upper and lower viscosity cut-offs are 10^{18} and 10^{25} Pa s. Thermal expansivity (α), specific heat (C_p) and thermal conductivity (k) are 3×10^{-5} $\mathrm{K^{-1}}$, 1200 J $\mathrm{K^{-1}}$ $\mathrm{kg^{-1}}$, and 3.3 W $\mathrm{m^{-1}}$ $\mathrm{K^{-1}}$, respectively.

The choice of density of the cratonic block is a key parameter for destruction. It is quite challenging to estimate the density of the original craton before the destruction started. (Ye et al., 2021) used the in-situ single crystal diffraction method to obtain the pressure-temperature-volume distribution of the minerals obtained from the xenoliths of the eastern NCC. Further using a third order Birch-Murnaghan equation of state, Ye et al. (2021) estimated the density profile of the original craton (Fig. 2 B, black dashed line) at $\sim$ 200 Ma. We choose different density profiles (ρ_i) for cratons by varying their reference density (ρ_i^0) between 3400, 3300, and 3200 kg $\mathrm{m^{-3}}$ at 20 °C, respectively. The actual densities are calculated as $\rho_\mathrm{i} = \rho_\mathrm{i}^0(1 - \alpha\delta\mathrm{T})$, where α and δT are the thermal expansivity (3×10^{-5} $\mathrm{K^{-1}}$) and deviation of temperature from 20 °C. While the estimated density by Ye et al. (2021) falls within the range of 3280 to 3300 kg $\mathrm{m^{-3}}$ (Fig 2 B, black dashed line), our models show similar densities to the estimated value, ranging between 3180 and 3300 kg $\mathrm{m^{-3}}$ (Fig. 2 B). Each density model is tested with three different weakening rates (see next paragraph) to have 9 models (models M1-M9, Table S2). We also test a another 9 models including high density lower crust and weak mid-lithospheric discontinuity (models M10 - M18, Fig. 2 C, Table S2). The dense lower crust is added at 30-70 km depth in models M13- M15 and the mid-lithospheric discontinuity is added at 60-100 km depth in models M16-M18.

To approximate gradual hydration-induced weakening in the eastern part of the craton, we divide the cratonic lithosphere into six thin layers (Fig. 2 A). Each layer gradually transitions (Spang, Burton, et al., 2022) from a dry olivine rheology to a wet olivine rheology from bottom to top (Supplementary Table 1). This transition is deemed realistic based on the estimated high water content within the NCC (Xia, Liu, et al., 2013). Dry olivine rheology makes the craton highly viscous, with a viscosity exceeding 10^{24} Pa s, while wet olivine rheology results in a viscosity of less than 10^{22} Pa s. However, determining the exact timing of hydration of the cratonic lithosphere poses a significant challenge. While some studies (J. Liu et al., 2019) have estimated the timing of slab dynamics and craton destruction, there is no consensus on the duration required for craton hydration. Experimental studies have suggested a wide range of hydrogen diffusivities, ranging from 10^{-11} to 10^{-4} $\mathrm{m^2\,s^{-1}}$ (Demouchy et al., 2007; Demouchy, 2010; Kohlstedt & Mackwell, 1998). Demouchy (2010) predicted a diffusivity of 5.11×10^{-6} $\mathrm{m^2\,s^{-1}}$ to be a reasonable estimate for upper mantle conditions at 1200 °C. At this rate, water can diffuse through 100 km in approximately 60 Myr (Fig. 2 D). Several studies have suggested that the rate of hydration could be accelerated if it is controlled by carbonatite melts (Hammouda & Laporte, 2000; X. Wang et al., 2022), which are abundant in the NCC (Chen et al., 2016, 2017; X. Wang et al., 2022). Additionally, some recent hypotheses propose that water infiltration along the slab gap may have also influenced the rate of hydration weakening within the NCC (Z. Wang et al., 2023). Based on various calculations, we assume three different weakening rates, R1, R2, and R3 (Fig. 2 D), for the hydration of the eastern block of the NCC. R3 weakens each thin layer after 9 Myr, weakening the 100 km thick lithosphere within 54 Myr, closely matching the water diffusion timescale estimated by Demouchy (2010). R1 represents the fastest weakening rate, which can hydrate each thin layer in a time interval of 2.5 Myr, weakening the cratonic block within 15 Myr. This faster hydration rate still falls within the estimated range of water diffusion within the mantle (Fig. 2 D). To further assess the effect of weakening rates in our models, we choose another intermediate case R2, which can weaken the craton within 24 Myr. In the following sections, we analyze the results from 18 different models and discuss the factors contributing to craton destruction.

3 Results

3.1 Flat slab-induced hydration weakening and craton destruction

Amongst 18 models, we first discuss about model M2 that utilizes a fast weakening rate (R1, Fig. 2 D) and a reference density of 3300 kg m^{-3}. With this combination, the craton initially possesses a viscosity of the order of 10^{24} Pa s (Fig. 3) and a density between 3200−3250 kg m^{-3} (Fig. 2 B). The chosen density and viscosity maintain the craton in equilibrium above the mantle. The slab's density is slightly higher than that of the surrounding mantle, triggering subduction in the model. As the slab moves downward, it induces convection in the mantle, pushing the flow eastwards beneath the craton. Concurrently, as the craton gradually weakens from its base, mantle flow begins to shear the weakened cratonic material, leading to the formation of lithospheric drips. Some weakened sections of the craton sink towards the slab by mantle flow, where they are recycled into the mantle alongside the subducting slab. By 17 Myr, the cratonic lithosphere is completely weakened, and most lithospheric drips detach from the craton's base (Figs. 3 A, B, video S1). Within 40 Myr, majority cratonic lithosphere is recycled into mantle (Figs. 3 C, D).

We calculate the percentage of mantle material replacing cratonic material in the eastern block over time (Fig. 4). Initially, there is no mantle material replacing within the cratonic block. As cratonic material is removed, the void is replaced by upper mantle material. The increase in mantle material signifies the removal of cratonic material. From now on, we will use craton destruction or replacement of mantle material synonymously. Our tracking reveals that approximately 50% of mantle material replaces the original craton within just 20 Myr (Fig. 4 A, solid pink like for model M2), indicating a swift destruction of the majority of the craton. After the major destruction event, a slower process removes up to $\sim$ 70% of cratonic material within 40 Myr. The destruction further slows down due to the slab stagnating above lower mantle after $\sim$ 40 Myr (Figs. 3 C, D).

3.2 Effect of density and weakening rates

To comprehensively understand the mechanism of craton destruction, we conduct additional tests with different density profiles having reference densities 3400 kg m^{-3} (M1) and 3200 kg m^{-3} (M3) (Fig 2 A). Model M1 yields an actual density ranging between 3250 and 3300 kg m^{-3} (Fig. 2 A). Here, we observe $\sim$ 80 % replacement of mantle material within the eastern part of the craton within a time interval of around 20 Myr (Fig. 4 A, solid blue line). This suggests that a high density craton can experience more rapid destruction. Conversely, in model M3 (Table S2), where the craton density is lower than 3200 kg m^{-3}, only 5-10% of the craton has been destroyed (Fig. 4 A, solid cyan line), indicating that a craton with a density lower than 3200 kg m^{-3} may not undergo destruction even if it is weakened rapidly.

We further explore various hydration weakening rates using three sets of different density models. For models M1-M3, the fastest weakening rate (R1) is applied, i.e., weakening 100 km of craton within 15 Myr (Fig. 2 D). The intermediate weakening rate (R2), which weakens 100 km craton in 24 Myr, is applied in models M4-M6 (Table S2). Finally, the slowest weakening rate (R3), weakening 100 km of craton in 54 Myr, is used in models M7-M9 (Table S2). Regardless of the weakening rate, models with craton density below 3200 kg m^{-3} (models M3, M6, M9) show no significant craton destruction (Fig. 4 A, cyan lines). The amount of craton destruction is quite similar in the case of the R1 and R2 weakening rates. Both show rapid destruction of approximately 80% (models M1,

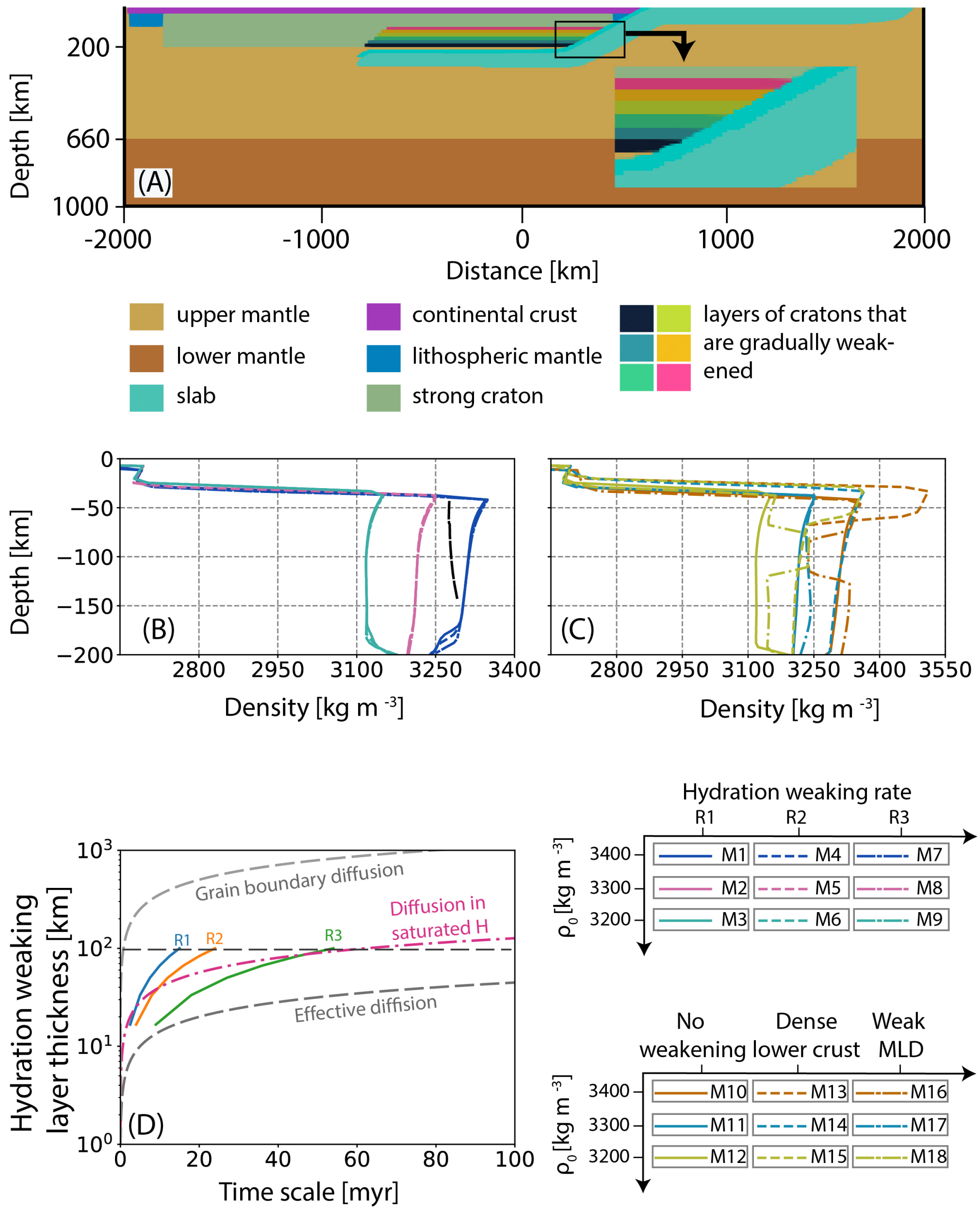

Figure 2. A: The geometry used for models M1-M9 is depicted, with each geological unit indicated by a specific color as indexed below. (B, C) The density profiles within the craton obtained from the 18 models is illustrated, with each line representing a specific model. The legend for B, C is provided in the lower right of the Figure. The black dashed line in (B) represents the density estimate of the NCC before destruction (Ye et al., 2021). (D) Hydration weakening rates calculated for different scenarios are presented. The Y-axis shows the thickness of a cratonic lithosphere that can be hydrated, while the X-axis represents the time required to hydrate that thickness of lithosphere. The top and bottom grey dashed lines represent the slowest and fastest weakening rates for hydration weakening calculated from the experimental data provided by Demouchy (2010). The pink dash-dot line represents the hydration weakening rate for upper mantle water diffusion rate in saturated conditions estimated by Demouchy (2010). R1, R2, and R3 denote the three hydration weakening rates utilized for this study.

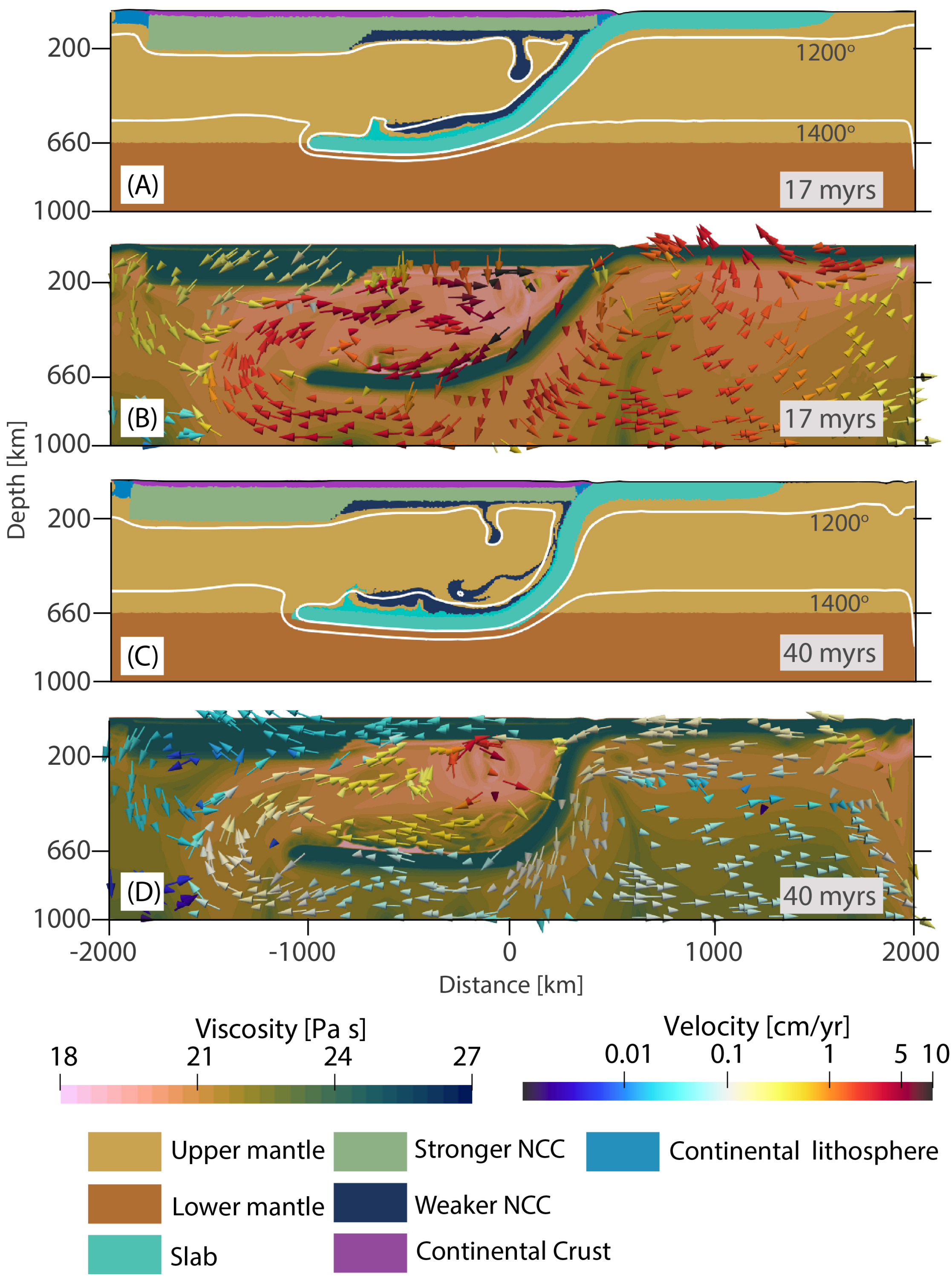

Figure 3. Snapshots of the NCC destruction from model M2 after 17 Myr (A-B) and 40 Myrs (C-D) respectively. Background colors in (A, C) represent geological units which are indexed below. Dark blue region indicates the weak craton which is forming lithospheric drips. White lines indicate isotherms of 1200°C and 1400°C. Background colors in (B,D) represent viscosity and the arrows represent velocity.

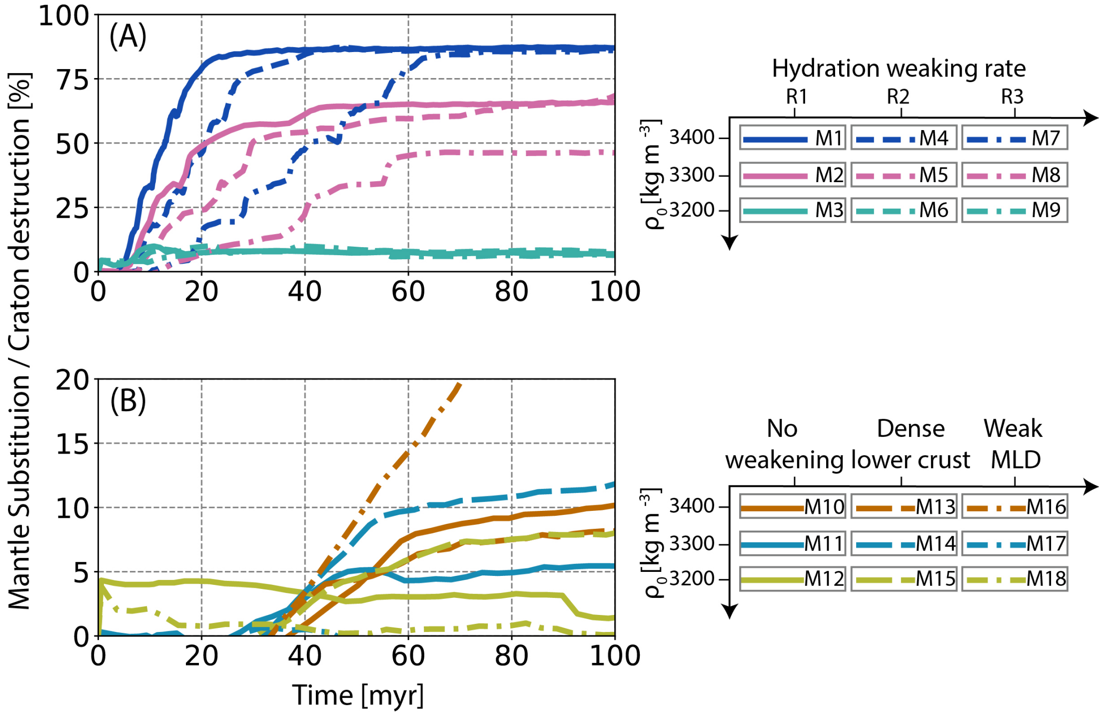

Figure 4. Temporal evolution of the substituted mantle percentage (equivalent to craton destruction) within the eastern block of the craton. Different lines representing different models are indexed beside each graph. Panel (A) shows models without hydration weakening, while panel (B) shows models with hydration weakening. Note the different scales of the Y-axes.

M4) and around 70% (models M2, M5) within approximately 20-40 Myr, respectively (Fig. 4 A). Craton destruction is slower with R3 weakening rate. With a reference density of 3400 kg m^{-3} in model M7, only 50 % craton is destroyed within 40 Myr, and for model M8 with reference density of 3300 kg m^{-3}, the destruction is only 25 % (Fig. 4 A).

3.3 Effect of flat slab, ecologitation, and mid-lithospheric discontinuity

In the subsequent models (M10-M18), we explore the impact of top-to-bottom destruction mechanisms without incorporating hydration-induced weakening. Initially, we focus solely on the influence of flat slab subduction without weakening the craton (models M10-M12). Despite the subducting slab causing significant mantle perturbation, the craton remains unaffected. Even when the craton is significantly denser than the underlying mantle (model M10), stability is maintained as long as its viscosity exceeds 10^{24} Pa s (Fig. S1). Tracking mantle substitution reveals minimal replacement of cratonic material by new mantle, with the cratons remaining unaffected in all three models (M10-M12) (Fig. 4 B, solid lines).

Introducing a denser lower crust theoretically allows for the development of crustal drips capable of foundering through the underlying cratonic lithosphere and potentially destroying it (Gao et al., 2004). We investigate this scenario by incorporating an intentionally thick crust at a depth of 30 to 70 km, with densities reaching up to 3500 kg m^{-3} (models M13-M15, Table S2). Model M13 features the highest density lower crustal layer (3500 kg m^{-3}). Despite the high density, lower crustal foundering is not observed in this model (Fig. S2). Tracking mantle phases indicates that less than 10% of the mantle substitutes the densest cratonic material, with negligible material substitution in the other two models with dense lower crust (Fig. 4 B, dashed lines). This suggests that the presence of the lower crust cannot lead to craton destruction in our models.

In another scenario, we examine the effect of the weak mid-lithospheric discontinuity (MLD) (models M16-M18). The reference density (ρ_o) of the weak MLD is set at 3300 kg m^{-3}, and wet olivine rheology is imposed to weaken it. Similarly, we vary the craton's density in three models akin to previous models. In model M16, the craton's reference density is kept at 3400 kg m^{-3} (Table S2). The mantle replacement curve shows significant craton destruction for model M16. However, the craton delaminates beneath the weak MLD from its western part, making it inconsistent with the geological observations (Fig. S3). Craton destruction remains negligible in models M17-M18 (Fig. 4 B, dashdot lines).

4 Discussion

The destruction of the eastern part of the NCC has been widely acknowledged. Several mechanisms are proposed to understand the reasons for the destruction (Gao et al., 2004; J. Liu et al., 2019; Menzies et al., 1993; F.-Y. Wu et al., 2019; J. Zheng et al., 2005; Zhu et al., 2012) including hydration weakening, crustal foundering, and decoupling due to a weak MLD. It is crucial to emphasize that only the eastern-central part of the craton was subjected to destruction, while the western part remained intact. To determine the most viable mechanism for the NCC's destruction, numerical models are developed to simulate relevant geological scenarios.

Our results indicate that if cratons can be weakened rapidly (R1 or R2 weakening rate), slightly faster than the diffusive timescale of water in the upper mantle (R3), 50-80% of a craton can be destroyed within approximately 15-20 Myr, and 70-90% within around 40 Myr. These findings are consistent with geological observations that suggested rapid destruction of the NCC within 20-40 Myr (J. Liu et al., 2019; Chen et al., 2017). Accelerated hydration weakening could be an effect of rapid reaction between carbonatite melt and pyroxene minerals of the cratonic lithosphere (X. Wang et al., 2022) that can form potential pathways for water to diffuse through the craton. Previous studies indicated higher water content in the Cretaceous lithospheric mantle of the eastern part compared to the western counterpart (Xia, Liu, et al., 2013; Xia, Hao, et al., 2013). Besides subduction zone fluids, substantial carbonate sediments may have been introduced in this region (Chen et al., 2016; X. Wang et al., 2022), erupting as carbonatite magma and accelerating hydration weakening within the NCC (X. Wang et al., 2022).

We have observed that densities higher than the underlying mantle (~ 3200 kg m^{-3}) and viscosities of the order of 10^{22} Pa s are critical for the destruction of 70-90% of the craton in our models (M1, M2, M4, M5, M7, M8). Failure to meet either of these conditions does not lead to significant destruction (see Table S2). Even in the case where a craton's density exceeds that of the underlying mantle, but the viscosity remains of the order of 10^{24} Pa s, no lithospheric drips form (e.g., models M10, M13, M15). Conversely, when viscosity decreases below 10^{22} Pa s but the density does not surpass the underlying mantle (~ 3200 kg m^{-3}), the weakened craton remains intact in this short time of 100 Myr (e.g., models M3, M6, M9). Therefore, craton destruction is profoundly reliant on both parameters. The viscosity estimate aligns with previous studies indicating that cratons with viscosities of the order of 10^{23} to 10^{24} Pa s can endure for at least a few hundred million years (Paul et al., 2019; Paul & Ghosh, 2020).

For similar reasons, lower crustal foundering fails to destroy the craton in our models. Developing crustal instabilities through a highly viscous cratonic lithosphere, even with a thick and dense lower crust, proves unfeasible. The foundering of the lower crustal layer might be effective in active orogens like the Tibetan plateau (Houseman & Molnar, 1997), where the mantle beneath the lower crust is sufficiently hot and weak to initiate such crustal instabilities. Hence, our models do not support the hypothesis of exclusive lower crustal foundering leading to destruction.

Weak mid-lithospheric discontinuitie (MLD) has also proven ineffective in the NCC destruction in most instances, except when a denser craton is positioned beneath MLD (model M16). In such scenarios, viscous decoupling becomes more efficient, promoting the delamination of the dense cratonic root beneath the MLD. A similar type of craton modification has been proposed for the African craton (Z. Wang et al., 2017). However, due to the geometrical configuration, the eastern part of the North China Craton (NCC) was shielded by a flat slab, and destruction initiated from the western margin in presence of a weak MLD. This scenario does not agree with the geological observations, challenging the viability of the MLD-induced hypothesis in this case. A previous study modeled the destruction of the NCC using a weak MLD (Shi et al., 2020); however, they did not consider the presence of a flat slab, which could have shielded the eastern block for an extended period. Additionally, the status of 'weak' MLDs under cratons is highly debated (Z. Wang & Kusky, 2019), and further studies are required to determine whether a weak MLD even existed in this region during the Jurassic.

Based on all 18 models Models we suggest that hydration weakening and subsequent destruction is the most viable mechanism for the NCC desturction. We note that hydration and subsequent weakening are not explicitly modeled in our investigation. Instead, we use a simplified approximation to mimic the timescales of water transport and the effects of metasomatism, thus matching the potential of hydration weakening by first order. Furthermore, 2D models do not allow us to rule out craton destruction by trench-parallel motion. Our results do, however, suggest that material that is not dense enough or too viscous cannot be recycled within the time frame assumed for the NCC.

5 Conclusions

Our results demonstrate that density and viscosity of the lower cratonic lithosphere both have to meet critical conditions to allow for destruction. Only if the craton's density is higher than that of the underlying mantle and its viscosity is lower than 10^{22} Pa s, drips can form and sink into the mantle. Meeting these conditions, results in 70 - 90% destruction of the lower, eastern NCC. We find that top-to-bottom processes such as foundering due to a dense lower crust or delamination along a weak MLD fail to meet both critical conditions and result in a largely stable craton. In our models, only the bottom-to-top process of flat slab-induced hydration and subsequent weakening fulfills both conditions and is therefore the most viable explanation for the NCC destruction. To match the established destruction timescale of 20-40 Myr, the hydration of the eastern NCC needed to be sufficiently fast which was likely facilitated by subduction channel fluids and the abundant carbonatite melts.

6 Open Research

Numerical models were developed using the open source finite difference code LaMEM (https://github.com/UniMainzGeo/LaMEM). The model geometry is drawn using another open source MATLAB code geomIO (https://bitbucket.org/geomio/geomio/src/master/). The current version of geomIO used in this study can be downloaded from https://zenodo.org/records/10878180. Example LaMEM input file and geomIO files are uploaded in https://zenodo.org/records/10886215 and https://jyotirmoyp.github.io/research/craton/.

Acknowledgments
AS received funding from the DFG grant TH 2076/8-1. AP received funding from the DFG grant TH 2076/7-1. JP thanks Dr. Mahesh Halder for presubmission review of this manuscript. Publication cost is funded by Open Access Publishing Fund of the University of Bayreuth.

References

Bauville, A., & Baumann, T. S. (2019). geomio: An open-source MATLAB toolbox to create the initial configuration of 2-d/3-d thermo-mechanical simulations from 2-d vector drawings. *Geochemistry, Geophysics, Geosystems*, *20*(3), 1665–1675.

Chen, C., Liu, Y., Foley, S. F., Ducea, M. N., Geng, X., Zhang, W., ... Wang, Z. (2017). Carbonated sediment recycling and its contribution to lithospheric refertilization under the northern North China Craton. *Chemical Geology*, *466*, 641–653.

Chen, C., Liu, Y., Foley, S. F., Ducea, M. N., He, D., Hu, Z., ... Zong, K. (2016). Paleo-Asian oceanic slab under the North China craton revealed by carbonatites derived from subducted limestones. *Geology*, *44*(12), 1039–1042.

Conrad, C. P., & Lithgow-Bertelloni, C. (2006). Influence of continental roots and asthenosphere on plate-mantle coupling. *Geophysical Research Letters*, *33*(5).

Conrad, C. P., & Molnar, P. (1999). Convective instability of a boundary layer with temperature-and strain-rate-dependent viscosity in terms of 'available buoyancy'. *Geophysical Journal International*, *139*(1), 51–68.

Demouchy, S. (2010). Diffusion of hydrogen in olivine grain boundaries and implications for the survival of water-rich zones in the Earth's mantle. *Earth and Planetary Science Letters*, *295*(1-2), 305–313.

Demouchy, S., Mackwell, S. J., & Kohlstedt, D. L. (2007). Influence of hydrogen on Fe–Mg interdiffusion in (Mg, Fe) O and implications for Earth's lower mantle. *Contributions to Mineralogy and Petrology*, *154*(3), 279–289.

Gao, S., Rudnick, R. L., Yuan, H.-L., Liu, X.-M., Liu, Y.-S., Xu, W.-L., . . . Wang, Q.-H. (2004). Recycling lower continental crust in the North China craton. *Nature*, *432*(7019), 892–897.

Hammouda, T., & Laporte, D. (2000). Ultrafast mantle impregnation by carbonatite melts. *Geology*, *28*(3), 283–285.

Hirth, G., & Kohlstedt, D. (2003). Rheology of the upper mantle and the mantle wedge: A view from the experimentalists. *Geophysical monograph-american geophysical union*, *138*, 83–106.

Houseman, G. A., & Molnar, P. (1997). Gravitational (Rayleigh–Taylor) instability of a layer with non-linear viscosity and convective thinning of continental lithosphere. *Geophysical Journal International*, *128*(1), 125–150.

Kohlstedt, D. L., & Mackwell, S. J. (1998). Diffusion of hydrogen and intrinsic point defects in olivine. *Zeitschrift für physikalische Chemie*, *207*(1-2), 147–162.

Liao, J., & Gerya, T. (2014). Influence of lithospheric mantle stratification on craton extension: Insight from two-dimensional thermo-mechanical modeling. *Tectonophysics*, *631*, 50–64.

Liu, J., Cai, R., Pearson, D. G., & Scott, J. M. (2019). Thinning and destruction of the lithospheric mantle root beneath the North China Craton: A review. *Earth-Science Reviews*, *196*, 102873.

Liu, L., Liu, L., Xu, Y.-G., Xia, B., Ma, Q., & Menzies, M. (2019). Development of a dense cratonic keel prior to the destruction of the North China Craton: Constraints from sedimentary records and numerical simulation. *Journal of Geophysical Research: Solid Earth*, *124*(12), 13192–13206.

Mei, S., & Kohlstedt, D. (2000). Influence of water on plastic deformation of olivine aggregates: 2. Dislocation creep regime. *Journal of Geophysical Research: Solid Earth*, *105*(B9), 21471–21481.

Menzies, M. A., Fan, W., & Zhang, M. (1993). Palaeozoic and cenozoic lithoprobes and the loss of $>$ 120 km of Archaean lithosphere, Sino-Korean craton, China. *Geological Society, London, Special Publications*, *76*(1), 71–81.

Paul, J., & Ghosh, A. (2020). Evolution of cratons through the ages: A time-dependent study. *Earth and Planetary Science Letters*, *531*, 115962.

Paul, J., Ghosh, A., & Conrad, C. P. (2019). Traction and strain-rate at the base of the lithosphere: an insight into cratonic survival. *Geophysical Journal International*, *217*(2), 1024–1033.

Pusok, A. E., & Stegman, D. R. (2020). The convergence history of India-Eurasia records multiple subduction dynamics processes. *Science Advances*, *6*(19), eaaz8681.

Riel, N., Duarte, J. C., Almeida, J., Kaus, B. J., Rosas, F., Rojas-Agramonte, Y., & Popov, A. (2023). Subduction initiation triggered the Caribbean large igneous province. *Nature Communications*, *14*(1), 786.

Ritsema, J., van Heijst, H. J., & Woodhouse, J. H. (2004). Global transition zone tomography. *Journal of Geophysical Research: Solid Earth*, *109*(B2), doi:10.1029/2003JB002610.

Shi, Y.-N., Niu, F., Li, Z.-H., & Huangfu, P. (2020). Craton destruction links to the interaction between subduction and mid-lithospheric discontinuity: Implications for the eastern North China Craton. *Gondwana Research*, *83*, 49–62.

Spang, A., Baumann, T., & Kaus, B. J. (2022). Geodynamic modeling with uncertain initial geometries. *Geochemistry, Geophysics, Geosystems*, *23*(6), e2021GC010265.

Spang, A., Burton, M., Kaus, B. J., & Sigmundsson, F. (2022). Quantification of volcano deformation caused by volatile accumulation and release. *Geophysical Research Letters*, *49*(10), e2021GL097502.

Tang, J., Xu, W., Wang, F., & Ge, W. (2018). Subduction history of the Paleo-Pacific slab beneath Eurasian continent: Mesozoic-Paleogene magmatic records in Northeast Asia. *Science China Earth Sciences*, *61*, 527–559.

Tirel, C., Brun, J.-P., & Burov, E. (2008). Dynamics and structural development of metamorphic core complexes. *Journal of Geophysical Research: Solid Earth*, *113*(B4).

Wang, X., Zhang, J., Wang, C., Zong, K., & Xu, H. (2022). Experimental Constraint on Ca-Rich Carbonatite Melt-Peridotite Interaction and Implications for Lithospheric Mantle Modification Beneath the North China Craton. *Journal of Geophysical Research: Solid Earth*, *127*(9), e2022JB024769.

Wang, Z., & Kusky, T. M. (2019). The importance of a weak mid-lithospheric layer on the evolution of the cratonic lithosphere. *Earth-Science Reviews*, *190*, 557–569.

Wang, Z., Kusky, T. M., & Capitanio, F. A. (2017). Ancient continental lithosphere dislocated beneath ocean basins along the mid-lithosphere discontinuity: A hypothesis. *Geophysical Research Letters*, *44*(18), 9253–9260.

Wang, Z., Liu, L., Fu, Y., Zhao, L., Lin, J., Jin, Z., & Zheng, B. (2023). Multi-stage plate subduction controls intraplate volcanism and cratonic lithospheric thinning in Northeast Asia. *Earth-Science Reviews*, 104590.

Wu, F.-Y., Yang, J.-H., Xu, Y.-G., Wilde, S. A., & Walker, R. J. (2019). Destruction of the North China craton in the Mesozoic. *Annual Review of Earth and Planetary Sciences*, *47*, 173–195.

Wu, J. T.-J., Wu, J., & Okamoto, K. (2022). Intra-oceanic arc accretion along Northeast Asia during Early Cretaceous provides a plate tectonic context for North China craton destruction. *Earth-Science Reviews*, *226*, 103952.

Xia, Q., Hao, Y.-T., Liu, S.-C., Gu, X.-Y., & Feng, M. (2013). Water contents of the Cenozoic lithospheric mantle beneath the western part of the North China Craton: Peridotite xenolith constraints. *Gondwana Research*, *23*(1), 108–118.

Xia, Q., Liu, J., Liu, S.-C., Kovacs, I., Feng, M., & Dang, L. (2013). High water content in Mesozoic primitive basalts of the North China Craton and implications on the destruction of cratonic mantle lithosphere. *Earth and Planetary Science Letters*, *361*, 85–97.

Xu, Y.-G. (2001). Thermo-tectonic destruction of the Archaean lithospheric keel beneath the Sino-Korean Craton in China: Evidence, timing and mechanism. *Physics and Chemistry of the Earth, Part A: Solid Earth and Geodesy*, *26*(9-10), 747–757.

Yang, J.-H., Wu, F.-Y., Wilde, S. A., Belousova, E., & Griffin, W. L. (2008). Mesozoic decratonization of the North China block. *Geology*, *36*(6), 467–470.

Ye, Z., Fan, D., Tang, Q., Xu, J., Zhang, D., & Zhou, W. (2021). Constraining the density evolution during destruction of the lithospheric mantle in the eastern North China Craton. *Gondwana Research*, *91*, 18–30.

Zheng, J., Sun, M., Zhou, M.-F., & Robinson, P. (2005). Trace elemental and PGE geochemical constraints of Mesozoic and Cenozoic peridotitic xenoliths on lithospheric evolution of the North China Craton. *Geochimica et Cosmochimica Acta*, *69*(13), 3401–3418.

Zheng, Y., Xu, Z., Zhao, Z., & Dai, L. (2018). Mesozoic mafic magmatism in North China: Implications for thinning and destruction of cratonic lithosphere. *Science China Earth Sciences*, *61*, 353–385.

Zheng, Y.-F., Xiao, W.-J., & Zhao, G. (2013). Introduction to tectonics of China. *Gondwana Research*, *23*(4), 1189–1206.

Zhu, R.-X., Yang, J.-H., & Wu, F.-Y. (2012). Timing of destruction of the North China Craton. *Lithos*, *149*, 51–60.

Flat slab-induced hydration weakening and destruction of the North China Craton

Jyotirmoy Paul, Arne Spang, Andrea Piccolo

Bayerisches Geoinstitut, Universität Bayreuth, 95447 Bayreuth, Germany

Key Points:

- Investigation of North China Craton (NCC) destruction with thermomechanical numerical models.
- Flat slab-induced hydration can sufficiently weaken eastern part of the North China Craton (NCC).
- Craton is destroyed if its density is higher than the underlying mantle and its viscosity is lower than 10^{22} Pa s.

Corresponding author: Jyotirmoy Paul, jyotirmoy.paul@uni-bayreuth.de

Abstract

In this study, we develop two dimensional (2-D) box models to identify the most viable reasons for the destruction of the North China Craton (NCC). We examine the role of flat slab-induced hydration, high-density lower crust, and weak mid-lithospheric discontinuity in our models. Results indicate that flat slab-induced hydration weakening of the eastern part of the NCC can lead to rapid craton destruction if hydration weakening rates are sufficiently fast. This accelerated hydration rate may be attributed to the extensive carbonatite magmatism within the eastern part of the NCC, facilitating a faster pathway for water diffusion throughout the craton. Craton destruction is contingent upon the craton's density exceeding the surrounding mantle density, and its viscosity decreasing below 10^{22} Pa s. We observe that the presence of a dense lower crust or a weak mid-lithospheric discontinuity fail to destroy the NCC unless it is weakened.

Plain Language Summary

Cratons, constituting the oldest part of Earth's lithosphere, often exceed 3 billion years in age. Despite continuous recycling due to plate-tectonics on Earth, cratons maintain tectonic stability owing to their viscosity, density, and thickness. Nevertheless, certain geological activities can lead to the partial or complete destruction of cratons. A prime example is the North China Craton (NCC), where the eastern half has undergone extensive thinning. The mechanism behind the NCC's destruction has been a subject of debate for over the last two decades. In this study, we develop numerical models to investigate the most viable geodynamic scenario for the destruction of the NCC. We find hydration weakening, induced by fluids from the subducting slab, is the key control for craton destuction. Geological evidence indicates the flattening of the subducting slab during the Jurassic period. The presence of a flat slab likely facilitated partial hydration of the eastern half of the craton, while the western half remained intact. Subsequently, the weakened eastern segment could have been destroyed due to underlying mantle flow if the craton possessed a density exceeding underlying mantle and a viscosity lower than 10^{22} Pa s.

1 Introduction

Destruction of the North China Craton (NCC) (F.-Y. Wu et al., 2019; J. T.-J. Wu et al., 2022; Y.-F. Zheng et al., 2013; Zhu et al., 2012) challenges the notion of immortal cratons in geological history. Geophysical evidence, including the global litihospheric thickness model (Conrad & Lithgow-Bertelloni, 2006) (Fig. 1 A), slow seismic velocity anomalies in tomography models (Ritsema et al., 2004)(Fig. 1 A), and geochemical observations from xenolith studies (Menzies et al., 1993; Xu, 2001; Yang et al., 2008; J. Zheng et al., 2005; Y. Zheng et al., 2018; Zhu et al., 2012), firmly establish that the eastern part of the North China Craton is thinner than its western counterpart. Prior $\sim$200 Ma (early Jurassic period), the entire craton existed with a passive margin boundary and a normal cratonic thickness of approximately 200 km (Z. Wang & Kusky, 2019, c.f.). After 200 Ma, the onset of paleo-Pacific subduction along the eastern margin of the NCC reactivated the craton margin (Tang et al., 2018). In the early Cretaceous period ($\sim$ 130 - 100 Ma), the eastern part of the craton thickness was reduced to around 100 km (Zhu et al., 2012; F.-Y. Wu et al., 2019; J. T.-J. Wu et al., 2022; J. Zheng et al., 2005; Y. Zheng et al., 2018; J. Liu et al., 2019). Although there is consensus regarding the extensive thinning of the NCC, the mechanism behind it remains a subject of debate.

Previous studies proposed a range of possible mechanisms that could destroy the eastern part of the NCC. The onset of paleo-Pacific subduction at the eastern margin of the NCC has been considered as one of the most likely reasons for craton destruction (Xu, 2001; J. Zheng et al., 2005). The nature of the subduction zone remained disputed for a long time until recently, when several studies proposed the existence of a flat slab in this region. F.-Y. Wu et al. (2019) showed an age reversal of igneous rocks along an east-west transect from the paleo-subduction zone to the middle of the craton (Fig. 1 B). Many of these igneous activities are associated with carbonatite intrusions, particularly from the eastern part of the NCC (Chen et al., 2016, 2017; X. Wang et al., 2022). During the late Triassic and Jurassic periods, magmatic activities moved towards the continental interior, and in the Cretaceous period, magmatism migrated towards the sea (Fig. 1 C). This reversal is interpreted as the onset of westward flat subduction of the Paleo-Pacific slab around 200 Ma, followed by slab rollback at approximately 160 - 140 Ma (Y. Zheng et al., 2018; J. Liu et al., 2019; F.-Y. Wu et al., 2019; J. T.-J. Wu et al., 2022) (Fig. 1 C). The presence of a flat slab could have hydrated the eastern part of the craton (Fig. 1 C, hatched region) (F.-Y. Wu et al., 2019; J. T.-J. Wu et al., 2022; Y. Zheng et al., 2018), while the western block remained dry (Xia, Hao, et al., 2013). Xia, Liu, et al. (2013) studied the clinopyroxene samples of early Cretaceous basalts from the Feixian region (Fig. 1 A) and found high water content within them. They estimated that such high water content in clinopyroxene samples is possible only if the cratonic mantle contained at least 1000 ppm water before $\sim$ 120 Ma. Such high water content can change the 'dry' olivine rheology to 'wet' olivine (Hirth & Kohlstedt, 2003; Mei & Kohlstedt, 2000; Xia, Liu, et al., 2013), significantly reducing the overall viscosity of the lithospheric mantle. Weaker cratons potentially form lithospheric drips depending on their 'available buoyancy' (Conrad & Molnar, 1999), and those drips are removed gradually. Y. Zheng et al. (2018) attributed the NCC destruction to such a bottom-to-top process.

There are other mechanisms that could also have destroyed the NCC. Due to high pressure and temperature, dense eclogites are formed within the thick lower crust. This dense layer initiates a gravitational instability which can delaminate the crust, and eventually destroy the cratonic lithosphere by a process called foundering (Gao et al., 2004). Other studies have suggested the presence of a weak mid-lithospheric discontinuity (MLD) as another potential reason for craton destruction (Liao & Gerya, 2014; L. Liu et al., 2019; Shi et al., 2020; Z. Wang & Kusky, 2019). Unlike the slab-induced process, these two destruction mechanisms are top-to-bottom processes, where craton destruction initiates at the top margin (Y. Zheng et al., 2018).

In this study, we use thermomechanical numerical models to investigate the evolution and destruction of the North China Craton. We investigate several scenarios to test their mechanical and geodynamical viability. Though our primary focus is to understand flat slab-induced destruction, we also examine cases in the presence of a dense lower crustal layer and a weak mid-lithospheric discontinuity. We explore different parameters, including density, viscosity, and the rate of hydration to support our arguments. We calibrate the timing of destruction with geologically observed data.

2 Geodynamic model

We develop time-dependent geodynamic models, using the thermomechanical finite differences code LaMEM (Kaus et al., 2016, details in supplementary text S1) which is routinely used to model subduction dynamics (Pusok & Stegman, 2020; Riel et al., 2023). Our 2D model domain consists of a Cartesian box of 4000$\times$1000 km (Fig. 2A) and is built with geomIO (Bauville & Baumann, 2019; Spang, Baumann, & Kaus, 2022). The continental block comprises a 40 km thick continental crust, followed by a thick continental lithosphere down to 100 km and a cratonic lithosphere root extending to a depth of 200 km, with a width of 2000 km (Fig. 2 A). Below the continental lithosphere, the upper mantle extends to 660 km depth, and the lower mantle to 1000 km. Each layer is distinguished by a specific rheology given in supplementary table S1 (Hirth & Kohlstedt, 2003; Tirel et al., 2008). To simulate the paleo-Pacific subduction zone, we place a flat slab along the eastern margin of the craton following the approach of F.-Y. Wu et al. (2019) (Figs. 1 C, 2 A). The flat slab extends to the middle of the craton's width,

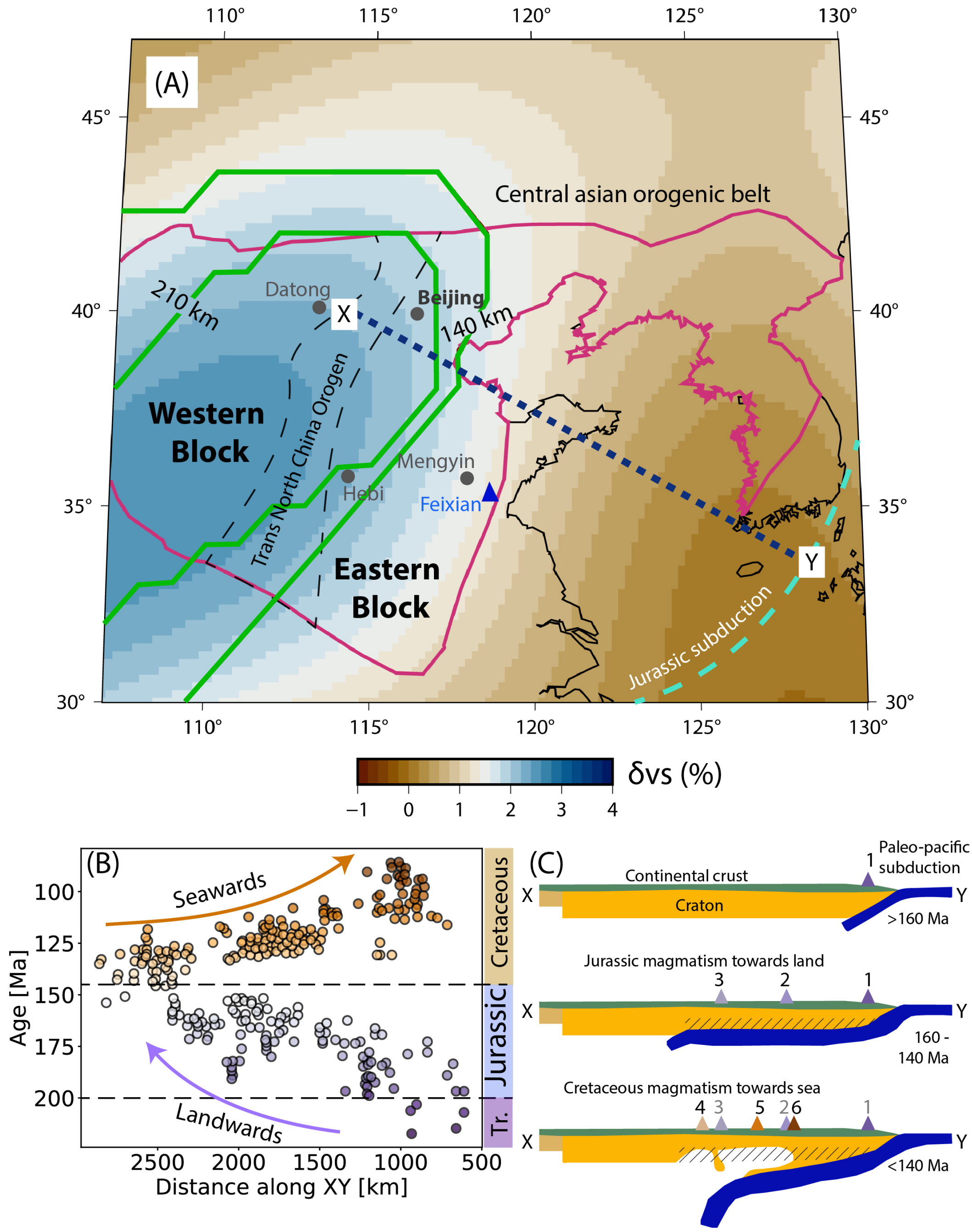

Figure 1. (A) Location of the North China Craton (NCC) marked by pink boundary. The western and eastern blocks of the NCC are separated by the trans North China orogen. The background colors in the Figure represent the shear wave velocity anomaly from the S20RTS tomography model (Ritsema et al., 2004), and the green lines are the contours of lithosphere thickness of 210 and 140 km, obtained from the global lithosphere thickness model of Conrad and Lithgow-Bertelloni (2006). Present-day coastlines are in black. Several igneous rocks are dated along the X-Y transect (F.-Y. Wu et al., 2019; J. T.-J. Wu et al., 2022). (B) Age distribution of igneous rocks along X-Y transect extracted and complied from (Z. Wang & Kusky, 2019; J. T.-J. Wu et al., 2022). (C) Schematic diagram of destruction of North China Craton modified after J. Liu et al. (2019); F.-Y. Wu et al. (2019); J. T.-J. Wu et al. (2022). 1-6 represent progression of magmatic activity with time.

hypothetically dividing it into eastern and western part. The mantle flow dynamics are driven by the density anomaly of the slab and an additional inflow of 1-2 $\mathrm{cm\,yr^{-1}}$ from the eastern margin of our model. Additionally, a temperature difference of 1600 K between the top and the bottom of the model also contributes to the vigour of mantle flow. The upper and lower viscosity cut-offs are 10^{18} and 10^{25} Pa s. Thermal expansivity (α), specific heat (C_p) and thermal conductivity (k) are 3×10^{-5} K^{-1}, 1200 J K^{-1} kg^{-1}, and 3.3 W m^{-1} K^{-1}, respectively.

The choice of density of the cratonic block is a key parameter for destruction. It is quite challenging to estimate the density of the original craton before the destruction started. (Ye et al., 2021) used the in-situ single crystal diffraction method to obtain the pressure-temperature-volume distribution of the minerals obtained from the xenoliths of the eastern NCC. Further using a third order Birch-Murnaghan equation of state, Ye et al. (2021) estimated the density profile of the original craton (Fig. 2 B, black dashed line) at $\sim$ 200 Ma. We choose different density profiles (ρ_i) for cratons by varying their reference density (ρ_i^0) between 3400, 3300, and 3200 kg m^{-3} at 20 °C, respectively. The actual densities are calculated as $\rho_\mathrm{i} = \rho_\mathrm{i}^0(1 - \alpha\delta\mathrm{T})$, where α and δT are the thermal expansivity ($3{\times}10^{-5}$ K^{-1}) and deviation of temperature from 20 °C. While the estimated density by Ye et al. (2021) falls within the range of 3280 to 3300 kg m^{-3} (Fig 2 B, black dashed line), our models show similar densities to the estimated value, ranging between 3180 and 3300 kg m^{-3} (Fig. 2 B). Each density model is tested with three different weakening rates (see next paragraph) to have 9 models (models M1-M9, Table S2). We also test a another 9 models including high density lower crust and weak mid-lithospheric discontinuity (models M10 - M18, Fig. 2 C, Table S2). The dense lower crust is added at 30-70 km depth in models M13- M15 and the mid-lithospheric discontinuity is added at 60-100 km depth in models M16-M18.

To approximate gradual hydration-induced weakening in the eastern part of the craton, we divide the cratonic lithosphere into six thin layers (Fig. 2 A). Each layer gradually transitions (Spang, Burton, et al., 2022) from a dry olivine rheology to a wet olivine rheology from bottom to top (Supplementary Table 1). This transition is deemed realistic based on the estimated high water content within the NCC (Xia, Liu, et al., 2013). Dry olivine rheology makes the craton highly viscous, with a viscosity exceeding 10^{24} Pa s, while wet olivine rheology results in a viscosity of less than 10^{22} Pa s. However, determining the exact timing of hydration of the cratonic lithosphere poses a significant challenge. While some studies (J. Liu et al., 2019) have estimated the timing of slab dynamics and craton destruction, there is no consensus on the duration required for craton hydration. Experimental studies have suggested a wide range of hydrogen diffusivities, ranging from 10^{-11} to 10^{-4} $\mathrm{m^2\,s^{-1}}$ (Demouchy et al., 2007; Demouchy, 2010; Kohlstedt & Mackwell, 1998). Demouchy (2010) predicted a diffusivity of $5.11{\times}10^{-6}$ $\mathrm{m^2\,s^{-1}}$ to be a reasonable estimate for upper mantle conditions at 1200 °C. At this rate, water can diffuse through 100 km in approximately 60 Myr (Fig. 2 D). Several studies have suggested that the rate of hydration could be accelerated if it is controlled by carbonatite melts (Hammouda & Laporte, 2000; X. Wang et al., 2022), which are abundant in the NCC (Chen et al., 2016, 2017; X. Wang et al., 2022). Additionally, some recent hypotheses propose that water infiltration along the slab gap may have also influenced the rate of hydration weakening within the NCC (Z. Wang et al., 2023). Based on various calculations, we assume three different weakening rates, R1, R2, and R3 (Fig. 2 D), for the hydration of the eastern block of the NCC. R3 weakens each thin layer after 9 Myr, weakening the 100 km thick lithosphere within 54 Myr, closely matching the water diffusion timescale estimated by Demouchy (2010). R1 represents the fastest weakening rate, which can hydrate each thin layer in a time interval of 2.5 Myr, weakening the cratonic block within 15 Myr. This faster hydration rate still falls within the estimated range of water diffusion within the mantle (Fig. 2 D). To further assess the effect of weakening rates in our models, we choose another intermediate case R2, which can weaken the craton within 24 Myr. In the following sections, we analyze the results from 18 different models and discuss the factors contributing to craton destruction.

3 Results

3.1 Flat slab-induced hydration weakening and craton destruction

Amongst 18 models, we first discuss about model M2 that utilizes a fast weakening rate (R1, Fig. 2 D) and a reference density of 3300 kg m^{-3}. With this combination, the craton initially possesses a viscosity of the order of 10^{24} Pa s (Fig. 3) and a density between 3200−3250 kg m^{-3} (Fig. 2 B). The chosen density and viscosity maintain the craton in equilibrium above the mantle. The slab's density is slightly higher than that of the surrounding mantle, triggering subduction in the model. As the slab moves downward, it induces convection in the mantle, pushing the flow eastwards beneath the craton. Concurrently, as the craton gradually weakens from its base, mantle flow begins to shear the weakened cratonic material, leading to the formation of lithospheric drips. Some weakened sections of the craton sink towards the slab by mantle flow, where they are recycled into the mantle alongside the subducting slab. By 17 Myr, the cratonic lithosphere is completely weakened, and most lithospheric drips detach from the craton's base (Figs. 3 A, B, video S1). Within 40 Myr, majority cratonic lithosphere is recycled into mantle (Figs. 3 C, D).

We calculate the percentage of mantle material replacing cratonic material in the eastern block over time (Fig. 4). Initially, there is no mantle material replacing within the cratonic block. As cratonic material is removed, the void is replaced by upper mantle material. The increase in mantle material signifies the removal of cratonic material. From now on, we will use craton destruction or replacement of mantle material synonymously. Our tracking reveals that approximately 50% of mantle material replaces the original craton within just 20 Myr (Fig. 4 A, solid pink like for model M2), indicating a swift destruction of the majority of the craton. After the major destruction event, a slower process removes up to $\sim$ 70% of cratonic material within 40 Myr. The destruction further slows down due to the slab stagnating above lower mantle after $\sim$ 40 Myr (Figs. 3 C, D).

3.2 Effect of density and weakening rates

To comprehensively understand the mechanism of craton destruction, we conduct additional tests with different density profiles having reference densities 3400 kg m^{-3} (M1) and 3200 kg m^{-3} (M3) (Fig 2 A). Model M1 yields an actual density ranging between 3250 and 3300 kg m^{-3} (Fig. 2 A). Here, we observe $\sim$ 80 % replacement of mantle material within the eastern part of the craton within a time interval of around 20 Myr (Fig. 4 A, solid blue line). This suggests that a high density craton can experience more rapid destruction. Conversely, in model M3 (Table S2), where the craton density is lower than 3200 kg m^{-3}, only 5-10% of the craton has been destroyed (Fig. 4 A, solid cyan line), indicating that a craton with a density lower than 3200 kg m^{-3} may not undergo destruction even if it is weakened rapidly.

We further explore various hydration weakening rates using three sets of different density models. For models M1-M3, the fastest weakening rate (R1) is applied, i.e., weakening 100 km of craton within 15 Myr (Fig. 2 D). The intermediate weakening rate (R2), which weakens 100 km craton in 24 Myr, is applied in models M4-M6 (Table S2). Finally, the slowest weakening rate (R3), weakening 100 km of craton in 54 Myr, is used in models M7-M9 (Table S2). Regardless of the weakening rate, models with craton density below 3200 kg m^{-3} (models M3, M6, M9) show no significant craton destruction (Fig. 4 A, cyan lines). The amount of craton destruction is quite similar in the case of the R1 and R2 weakening rates. Both show rapid destruction of approximately 80% (models M1,

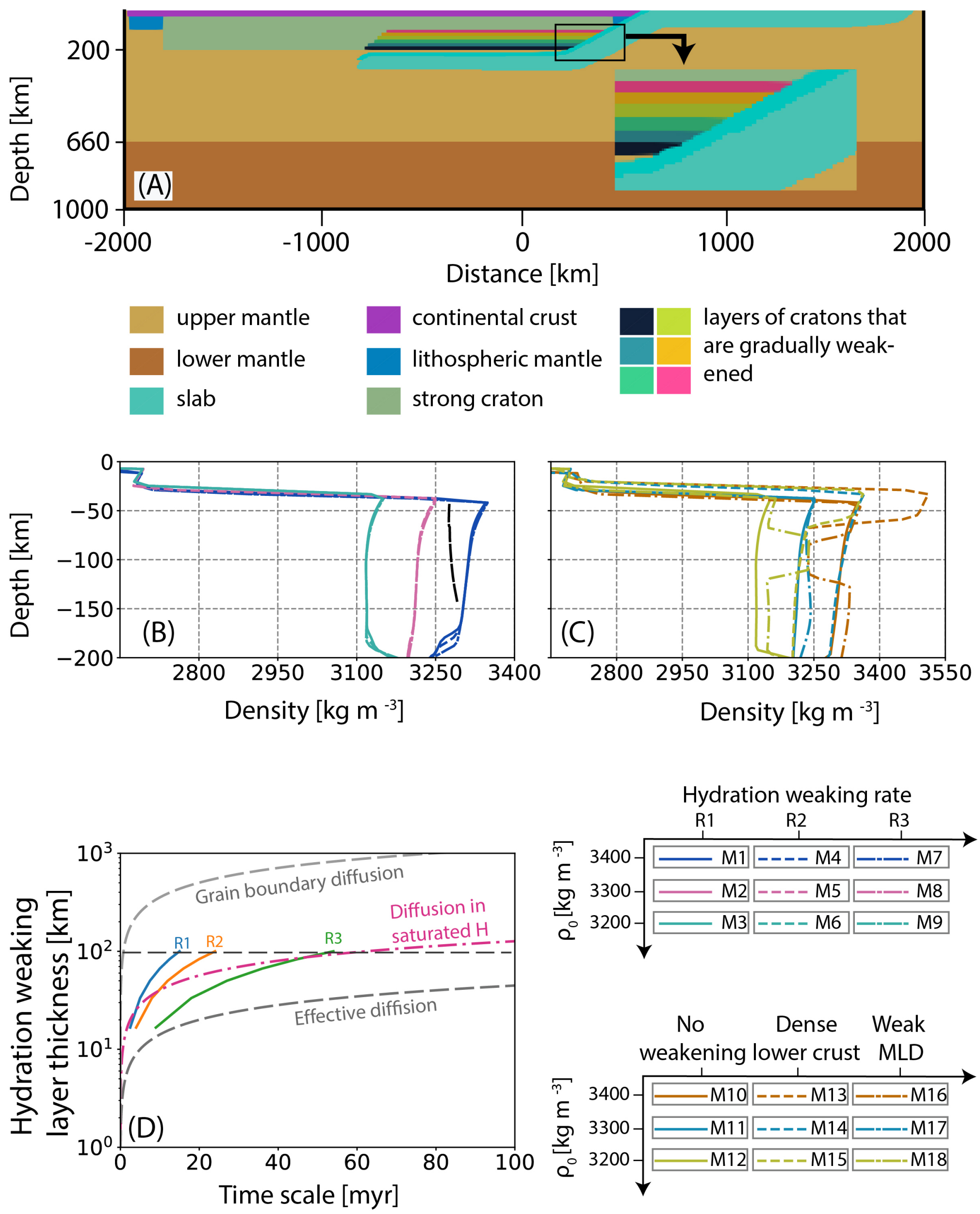

Figure 2. A: The geometry used for models M1-M9 is depicted, with each geological unit indicated by a specific color as indexed below. (B, C) The density profiles within the craton obtained from the 18 models is illustrated, with each line representing a specific model. The legend for B, C is provided in the lower right of the Figure. The black dashed line in (B) represents the density estimate of the NCC before destruction (Ye et al., 2021). (D) Hydration weakening rates calculated for different scenarios are presented. The Y-axis shows the thickness of a cratonic lithosphere that can be hydrated, while the X-axis represents the time required to hydrate that thickness of lithosphere. The top and bottom grey dashed lines represent the slowest and fastest weakening rates for hydration weakening calculated from the experimental data provided by Demouchy (2010). The pink dash-dot line represents the hydration weakening rate for upper mantle water diffusion rate in saturated conditions estimated by Demouchy (2010). R1, R2, and R3 denote the three hydration weakening rates utilized for this study.

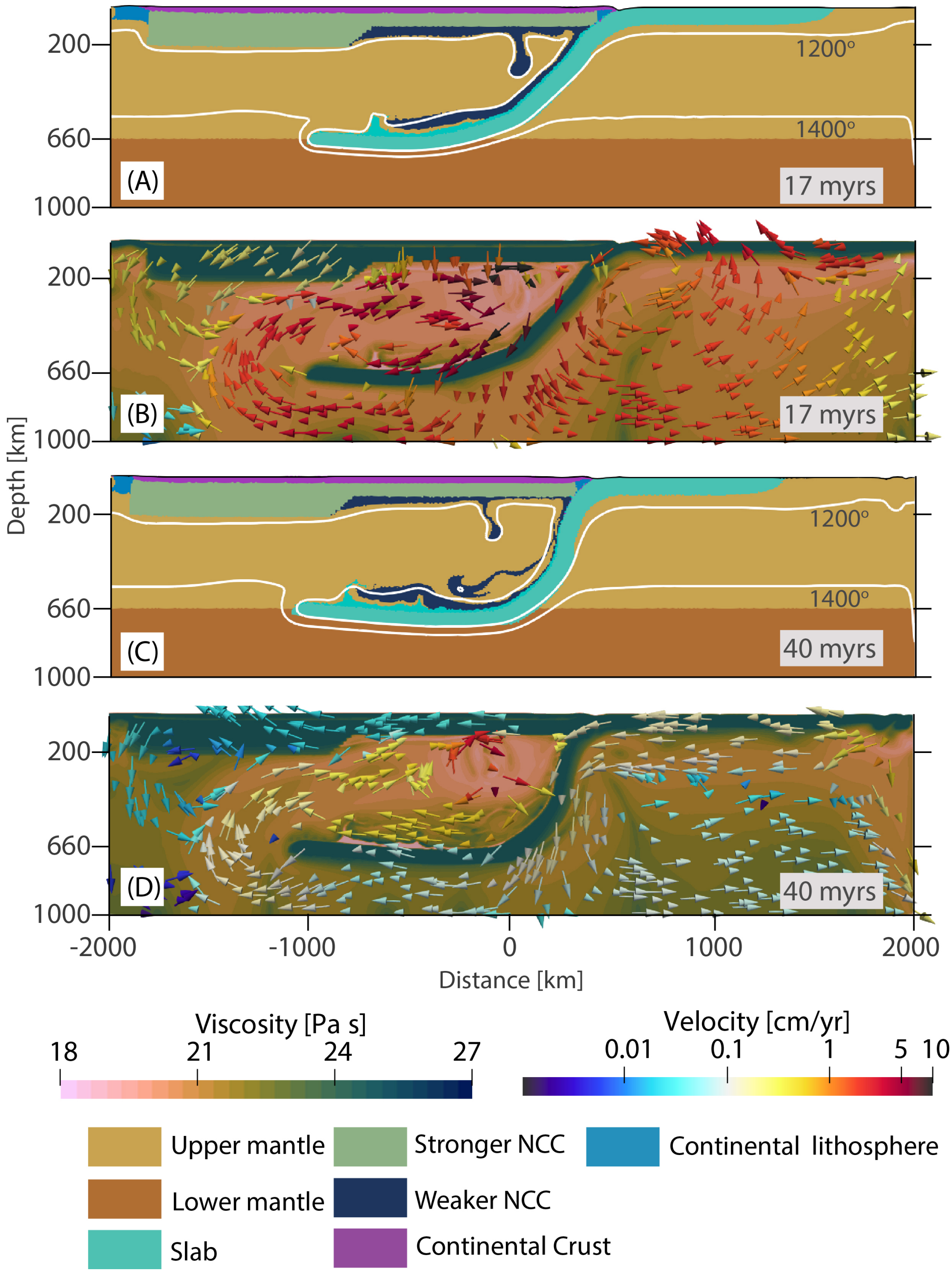

Figure 3. Snapshots of the NCC destruction from model M2 after 17 Myr (A-B) and 40 Myrs (C-D) respectively. Background colors in (A, C) represent geological units which are indexed below. Dark blue region indicates the weak craton which is forming lithospheric drips. White lines indicate isotherms of 1200°C and 1400°C. Background colors in (B,D) represent viscosity and the arrows represent velocity.

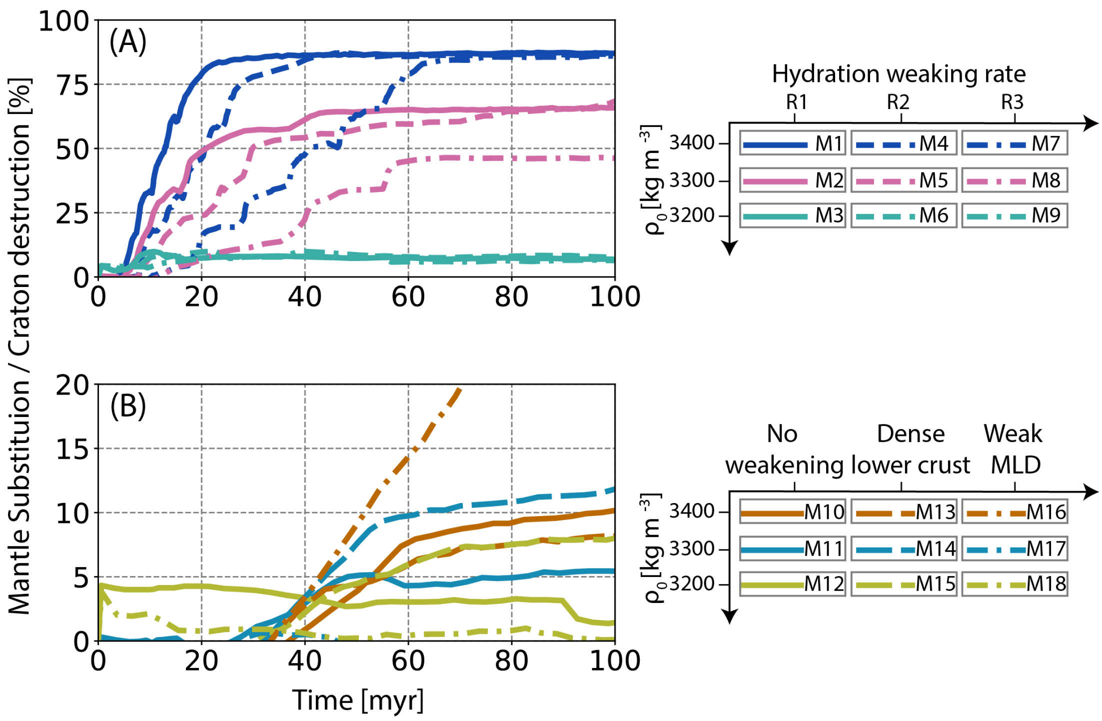

Figure 4. Temporal evolution of the substituted mantle percentage (equivalent to craton destruction) within the eastern block of the craton. Different lines representing different models are indexed beside each graph. Panel (A) shows models without hydration weakening, while panel (B) shows models with hydration weakening. Note the different scales of the Y-axes.

M4) and around 70% (models M2, M5) within approximately 20-40 Myr, respectively (Fig. 4 A). Craton destruction is slower with R3 weakening rate. With a reference density of 3400 kg m^{-3} in model M7, only 50 % craton is destroyed within 40 Myr, and for model M8 with reference density of 3300 kg m^{-3}, the destruction is only 25 % (Fig. 4 A).

3.3 Effect of flat slab, ecologitation, and mid-lithospheric discontinuity

In the subsequent models (M10-M18), we explore the impact of top-to-bottom destruction mechanisms without incorporating hydration-induced weakening. Initially, we focus solely on the influence of flat slab subduction without weakening the craton (models M10-M12). Despite the subducting slab causing significant mantle perturbation, the craton remains unaffected. Even when the craton is significantly denser than the underlying mantle (model M10), stability is maintained as long as its viscosity exceeds 10^{24} Pa s (Fig. S1). Tracking mantle substitution reveals minimal replacement of cratonic material by new mantle, with the cratons remaining unaffected in all three models (M10-M12) (Fig. 4 B, solid lines).

Introducing a denser lower crust theoretically allows for the development of crustal drips capable of foundering through the underlying cratonic lithosphere and potentially destroying it (Gao et al., 2004). We investigate this scenario by incorporating an intentionally thick crust at a depth of 30 to 70 km, with densities reaching up to 3500 kg m^{-3} (models M13-M15, Table S2). Model M13 features the highest density lower crustal layer (3500 kg m^{-3}). Despite the high density, lower crustal foundering is not observed in this model (Fig. S2). Tracking mantle phases indicates that less than 10% of the mantle substitutes the densest cratonic material, with negligible material substitution in the other two models with dense lower crust (Fig. 4 B, dashed lines). This suggests that the presence of the lower crust cannot lead to craton destruction in our models.

In another scenario, we examine the effect of the weak mid-lithospheric discontinuity (MLD) (models M16-M18). The reference density (ρ_o) of the weak MLD is set at 3300 kg m^{-3}, and wet olivine rheology is imposed to weaken it. Similarly, we vary the craton's density in three models akin to previous models. In model M16, the craton's reference density is kept at 3400 kg m^{-3} (Table S2). The mantle replacement curve shows significant craton destruction for model M16. However, the craton delaminates beneath the weak MLD from its western part, making it inconsistent with the geological observations (Fig. S3). Craton destruction remains negligible in models M17-M18 (Fig. 4 B, dashdot lines).

4 Discussion

The destruction of the eastern part of the NCC has been widely acknowledged. Several mechanisms are proposed to understand the reasons for the destruction (Gao et al., 2004; J. Liu et al., 2019; Menzies et al., 1993; F.-Y. Wu et al., 2019; J. Zheng et al., 2005; Zhu et al., 2012) including hydration weakening, crustal foundering, and decoupling due to a weak MLD. It is crucial to emphasize that only the eastern-central part of the craton was subjected to destruction, while the western part remained intact. To determine the most viable mechanism for the NCC's destruction, numerical models are developed to simulate relevant geological scenarios.

Our results indicate that if cratons can be weakened rapidly (R1 or R2 weakening rate), slightly faster than the diffusive timescale of water in the upper mantle (R3), 50-80% of a craton can be destroyed within approximately 15-20 Myr, and 70-90% within around 40 Myr. These findings are consistent with geological observations that suggested rapid destruction of the NCC within 20-40 Myr (J. Liu et al., 2019; Chen et al., 2017). Accelerated hydration weakening could be an effect of rapid reaction between carbonatite melt and pyroxene minerals of the cratonic lithosphere (X. Wang et al., 2022) that can form potential pathways for water to diffuse through the craton. Previous studies indicated higher water content in the Cretaceous lithospheric mantle of the eastern part compared to the western counterpart (Xia, Liu, et al., 2013; Xia, Hao, et al., 2013). Besides subduction zone fluids, substantial carbonate sediments may have been introduced in this region (Chen et al., 2016; X. Wang et al., 2022), erupting as carbonatite magma and accelerating hydration weakening within the NCC (X. Wang et al., 2022).

We have observed that densities higher than the underlying mantle (~ 3200 kg m^{-3}) and viscosities of the order of 10^{22} Pa s are critical for the destruction of 70-90% of the craton in our models (M1, M2, M4, M5, M7, M8). Failure to meet either of these conditions does not lead to significant destruction (see Table S2). Even in the case where a craton's density exceeds that of the underlying mantle, but the viscosity remains of the order of 10^{24} Pa s, no lithospheric drips form (e.g., models M10, M13, M15). Conversely, when viscosity decreases below 10^{22} Pa s but the density does not surpass the underlying mantle (~ 3200 kg m^{-3}), the weakened craton remains intact in this short time of 100 Myr (e.g., models M3, M6, M9). Therefore, craton destruction is profoundly reliant on both parameters. The viscosity estimate aligns with previous studies indicating that cratons with viscosities of the order of 10^{23} to 10^{24} Pa s can endure for at least a few hundred million years (Paul et al., 2019; Paul & Ghosh, 2020).

For similar reasons, lower crustal foundering fails to destroy the craton in our models. Developing crustal instabilities through a highly viscous cratonic lithosphere, even with a thick and dense lower crust, proves unfeasible. The foundering of the lower crustal layer might be effective in active orogens like the Tibetan plateau (Houseman & Molnar, 1997), where the mantle beneath the lower crust is sufficiently hot and weak to initiate such crustal instabilities. Hence, our models do not support the hypothesis of exclusive lower crustal foundering leading to destruction.

Weak mid-lithospheric discontinuitie (MLD) has also proven ineffective in the NCC destruction in most instances, except when a denser craton is positioned beneath MLD (model M16). In such scenarios, viscous decoupling becomes more efficient, promoting the delamination of the dense cratonic root beneath the MLD. A similar type of craton modification has been proposed for the African craton (Z. Wang et al., 2017). However, due to the geometrical configuration, the eastern part of the North China Craton (NCC) was shielded by a flat slab, and destruction initiated from the western margin in presence of a weak MLD. This scenario does not agree with the geological observations, challenging the viability of the MLD-induced hypothesis in this case. A previous study modeled the destruction of the NCC using a weak MLD (Shi et al., 2020); however, they did not consider the presence of a flat slab, which could have shielded the eastern block for an extended period. Additionally, the status of 'weak' MLDs under cratons is highly debated (Z. Wang & Kusky, 2019), and further studies are required to determine whether a weak MLD even existed in this region during the Jurassic.

Based on all 18 models Models we suggest that hydration weakening and subsequent destruction is the most viable mechanism for the NCC desturction. We note that hydration and subsequent weakening are not explicitly modeled in our investigation. Instead, we use a simplified approximation to mimic the timescales of water transport and the effects of metasomatism, thus matching the potential of hydration weakening by first order. Furthermore, 2D models do not allow us to rule out craton destruction by trench-parallel motion. Our results do, however, suggest that material that is not dense enough or too viscous cannot be recycled within the time frame assumed for the NCC.

5 Conclusions

Our results demonstrate that density and viscosity of the lower cratonic lithosphere both have to meet critical conditions to allow for destruction. Only if the craton's density is higher than that of the underlying mantle and its viscosity is lower than 10^{22} Pa s, drips can form and sink into the mantle. Meeting these conditions, results in 70 - 90% destruction of the lower, eastern NCC. We find that top-to-bottom processes such as foundering due to a dense lower crust or delamination along a weak MLD fail to meet both critical conditions and result in a largely stable craton. In our models, only the bottom-to-top process of flat slab-induced hydration and subsequent weakening fulfills both conditions and is therefore the most viable explanation for the NCC destruction. To match the established destruction timescale of 20-40 Myr, the hydration of the eastern NCC needed to be sufficiently fast which was likely facilitated by subduction channel fluids and the abundant carbonatite melts.

6 Open Research

Numerical models were developed using the open source finite difference code LaMEM (https://github.com/UniMainzGeo/LaMEM). The model geometry is drawn using another open source MATLAB code geomIO (https://bitbucket.org/geomio/geomio/src/master/). The current version of geomIO used in this study can be downloaded from https://zenodo.org/records/10878180. Example LaMEM input file and geomIO files are uploaded in https://zenodo.org/records/10886215 and https://jyotirmoyp.github.io/research/craton/.

Acknowledgments

AS received funding from the DFG grant TH 2076/8-1. AP received funding from the DFG grant TH 2076/7-1. JP thanks Dr. Mahesh Halder for presubmission review of this manuscript. Publication cost is funded by Open Access Publishing Fund of the University of Bayreuth.

References

Bauville, A., & Baumann, T. S. (2019). geomio: An open-source MATLAB toolbox to create the initial configuration of 2-d/3-d thermo-mechanical simulations from 2-d vector drawings. *Geochemistry, Geophysics, Geosystems*, *20*(3), 1665–1675.

Chen, C., Liu, Y., Foley, S. F., Ducea, M. N., Geng, X., Zhang, W., . . . Wang, Z. (2017). Carbonated sediment recycling and its contribution to lithospheric refertilization under the northern North China Craton. *Chemical Geology*, *466*, 641–653.

Chen, C., Liu, Y., Foley, S. F., Ducea, M. N., He, D., Hu, Z., . . . Zong, K. (2016). Paleo-Asian oceanic slab under the North China craton revealed by carbonatites derived from subducted limestones. *Geology*, *44*(12), 1039–1042.

Conrad, C. P., & Lithgow-Bertelloni, C. (2006). Influence of continental roots and asthenosphere on plate-mantle coupling. *Geophysical Research Letters*, *33*(5).

Conrad, C. P., & Molnar, P. (1999). Convective instability of a boundary layer with temperature-and strain-rate-dependent viscosity in terms of 'available buoyancy'. *Geophysical Journal International*, *139*(1), 51–68.

Demouchy, S. (2010). Diffusion of hydrogen in olivine grain boundaries and implications for the survival of water-rich zones in the Earth's mantle. *Earth and Planetary Science Letters*, *295*(1-2), 305–313.

Demouchy, S., Mackwell, S. J., & Kohlstedt, D. L. (2007). Influence of hydrogen on Fe–Mg interdiffusion in (Mg, Fe) O and implications for Earth's lower mantle. *Contributions to Mineralogy and Petrology*, *154*(3), 279–289.

Gao, S., Rudnick, R. L., Yuan, H.-L., Liu, X.-M., Liu, Y.-S., Xu, W.-L., … Wang, Q.-H. (2004). Recycling lower continental crust in the North China craton. *Nature*, *432*(7019), 892–897.

Hammouda, T., & Laporte, D. (2000). Ultrafast mantle impregnation by carbonatite melts. *Geology*, *28*(3), 283–285.

Hirth, G., & Kohlstedt, D. (2003). Rheology of the upper mantle and the mantle wedge: A view from the experimentalists. *Geophysical monograph-american geophysical union*, *138*, 83–106.

Houseman, G. A., & Molnar, P. (1997). Gravitational (Rayleigh–Taylor) instability of a layer with non-linear viscosity and convective thinning of continental lithosphere. *Geophysical Journal International*, *128*(1), 125–150.

Kohlstedt, D. L., & Mackwell, S. J. (1998). Diffusion of hydrogen and intrinsic point defects in olivine. *Zeitschrift für physikalische Chemie*, *207*(1-2), 147–162.

Liao, J., & Gerya, T. (2014). Influence of lithospheric mantle stratification on craton extension: Insight from two-dimensional thermo-mechanical modeling. *Tectonophysics*, *631*, 50–64.

Liu, J., Cai, R., Pearson, D. G., & Scott, J. M. (2019). Thinning and destruction of the lithospheric mantle root beneath the North China Craton: A review. *Earth-Science Reviews*, *196*, 102873.

Liu, L., Liu, L., Xu, Y.-G., Xia, B., Ma, Q., & Menzies, M. (2019). Development of a dense cratonic keel prior to the destruction of the North China Craton: Constraints from sedimentary records and numerical simulation. *Journal of Geophysical Research: Solid Earth*, *124*(12), 13192–13206.

Mei, S., & Kohlstedt, D. (2000). Influence of water on plastic deformation of olivine aggregates: 2. Dislocation creep regime. *Journal of Geophysical Research: Solid Earth*, *105*(B9), 21471–21481.

Menzies, M. A., Fan, W., & Zhang, M. (1993). Palaeozoic and cenozoic lithoprobes and the loss of $>$ 120 km of Archaean lithosphere, Sino-Korean craton, China. *Geological Society, London, Special Publications*, *76*(1), 71–81.

Paul, J., & Ghosh, A. (2020). Evolution of cratons through the ages: A time-dependent study. *Earth and Planetary Science Letters*, *531*, 115962.

Paul, J., Ghosh, A., & Conrad, C. P. (2019). Traction and strain-rate at the base of the lithosphere: an insight into cratonic survival. *Geophysical Journal International*, *217*(2), 1024–1033.

Pusok, A. E., & Stegman, D. R. (2020). The convergence history of India-Eurasia records multiple subduction dynamics processes. *Science Advances*, *6*(19), eaaz8681.

Riel, N., Duarte, J. C., Almeida, J., Kaus, B. J., Rosas, F., Rojas-Agramonte, Y., & Popov, A. (2023). Subduction initiation triggered the Caribbean large igneous province. *Nature Communications*, *14*(1), 786.

Ritsema, J., van Heijst, H. J., & Woodhouse, J. H. (2004). Global transition zone tomography. *Journal of Geophysical Research: Solid Earth*, *109*(B2), doi:10.1029/2003JB002610.

Shi, Y.-N., Niu, F., Li, Z.-H., & Huangfu, P. (2020). Craton destruction links to the interaction between subduction and mid-lithospheric discontinuity: Implications for the eastern North China Craton. *Gondwana Research*, *83*, 49–62.

Spang, A., Baumann, T., & Kaus, B. J. (2022). Geodynamic modeling with uncertain initial geometries. *Geochemistry, Geophysics, Geosystems*, *23*(6), e2021GC010265.

Spang, A., Burton, M., Kaus, B. J., & Sigmundsson, F. (2022). Quantification of volcano deformation caused by volatile accumulation and release. *Geophysical Research Letters*, *49*(10), e2021GL097502.

Tang, J., Xu, W., Wang, F., & Ge, W. (2018). Subduction history of the Paleo-Pacific slab beneath Eurasian continent: Mesozoic-Paleogene magmatic records in Northeast Asia. *Science China Earth Sciences*, *61*, 527–559.

Tirel, C., Brun, J.-P., & Burov, E. (2008). Dynamics and structural development of metamorphic core complexes. *Journal of Geophysical Research: Solid Earth*, *113*(B4).

Wang, X., Zhang, J., Wang, C., Zong, K., & Xu, H. (2022). Experimental Constraint on Ca-Rich Carbonatite Melt-Peridotite Interaction and Implications for Lithospheric Mantle Modification Beneath the North China Craton. *Journal of Geophysical Research: Solid Earth*, *127*(9), e2022JB024769.

Wang, Z., & Kusky, T. M. (2019). The importance of a weak mid-lithospheric layer on the evolution of the cratonic lithosphere. *Earth-Science Reviews*, *190*, 557–569.

Wang, Z., Kusky, T. M., & Capitanio, F. A. (2017). Ancient continental lithosphere dislocated beneath ocean basins along the mid-lithosphere discontinuity: A hypothesis. *Geophysical Research Letters*, *44*(18), 9253–9260.

Wang, Z., Liu, L., Fu, Y., Zhao, L., Lin, J., Jin, Z., & Zheng, B. (2023). Multi-stage plate subduction controls intraplate volcanism and cratonic lithospheric thinning in Northeast Asia. *Earth-Science Reviews*, 104590.

Wu, F.-Y., Yang, J.-H., Xu, Y.-G., Wilde, S. A., & Walker, R. J. (2019). Destruction of the North China craton in the Mesozoic. *Annual Review of Earth and Planetary Sciences*, *47*, 173–195.

Wu, J. T.-J., Wu, J., & Okamoto, K. (2022). Intra-oceanic arc accretion along Northeast Asia during Early Cretaceous provides a plate tectonic context for North China craton destruction. *Earth-Science Reviews*, *226*, 103952.

Xia, Q., Hao, Y.-T., Liu, S.-C., Gu, X.-Y., & Feng, M. (2013). Water contents of the Cenozoic lithospheric mantle beneath the western part of the North China Craton: Peridotite xenolith constraints. *Gondwana Research*, *23*(1), 108–118.

Xia, Q., Liu, J., Liu, S.-C., Kovacs, I., Feng, M., & Dang, L. (2013). High water content in Mesozoic primitive basalts of the North China Craton and implications on the destruction of cratonic mantle lithosphere. *Earth and Planetary Science Letters*, *361*, 85–97.

Xu, Y.-G. (2001). Thermo-tectonic destruction of the Archaean lithospheric keel beneath the Sino-Korean Craton in China: Evidence, timing and mechanism. *Physics and Chemistry of the Earth, Part A: Solid Earth and Geodesy*, *26*(9-10), 747–757.

Yang, J.-H., Wu, F.-Y., Wilde, S. A., Belousova, E., & Griffin, W. L. (2008). Mesozoic decratonization of the North China block. *Geology*, *36*(6), 467–470.

Ye, Z., Fan, D., Tang, Q., Xu, J., Zhang, D., & Zhou, W. (2021). Constraining the density evolution during destruction of the lithospheric mantle in the eastern North China Craton. *Gondwana Research*, *91*, 18–30.

Zheng, J., Sun, M., Zhou, M.-F., & Robinson, P. (2005). Trace elemental and PGE geochemical constraints of Mesozoic and Cenozoic peridotitic xenoliths on lithospheric evolution of the North China Craton. *Geochimica et Cosmochimica Acta*, *69*(13), 3401–3418.

Zheng, Y., Xu, Z., Zhao, Z., & Dai, L. (2018). Mesozoic mafic magmatism in North China: Implications for thinning and destruction of cratonic lithosphere. *Science China Earth Sciences*, *61*, 353–385.

Zheng, Y.-F., Xiao, W.-J., & Zhao, G. (2013). Introduction to tectonics of China. *Gondwana Research*, *23*(4), 1189–1206.

Zhu, R.-X., Yang, J.-H., & Wu, F.-Y. (2012). Timing of destruction of the North China Craton. *Lithos*, *149*, 51–60.

Supporting Information for "Flat slab-induced hydration weakening and destruction of the North China Craton"

Jyotirmoy Paul, Arne Spang, Andrea Piccolo

Bayerisches Geoinstitut, Universität Bayreuth, 95447 Bayreuth, Germany

Contents of this file

1. Text S1
2. Tables S1 to S2
3. Figures S1 to S3

Text S1. Thermomechanical Code

The thermomechanical finite differences code LaMEM (Kaus et al., 2016) solves for the conservation of momentum, mass and energy (eq. 1-3), using a staggered grid in combination with a marker-in-cell approach (Harlow & Welch, 1965).

$$\frac{\partial \tau_{ij}}{\partial x_j} - \frac{\partial P}{\partial x_i} + \rho g_i = 0 \tag{1}$$

$$\frac{\partial v_i}{\partial x_i} = 0 \tag{2}$$

$$\rho C_p \frac{DT}{Dt} = \frac{\partial}{\partial x_i}\left(k\frac{\partial T}{\partial x_i}\right) + H \tag{3}$$

τ_{ij} is the Cauchy stress deviator, $x_i (i = 1, 2, 3)$ denotes the Cartesian coordinates, P is pressure (positive in compression), ρ density, g_i gravitational acceleration, v_i the velocity vector, C_p the specific heat capacity, T the temperature, k the thermal conductivity, H the volumetric heat source and D/Dt is the material time derivative. Free slip conditions are applied to the boundaries of the model domain, allowing movement parallel to the domain edges while setting perpendicular velocities to 0 (with the exception of the oceanic plate inflow on the right boundary). At the top of the setup, we include sticky air above the stabilized free surface (Duretz et al., 2011; Kaus et al., 2010). The rocks are characterized by a temperature- and strain rate-dependent visco-elasto-plastic rheology where the strain rate is the sum of the elastic, viscous and plastic components:

$$\dot{\varepsilon}_{ij} = \dot{\varepsilon}_{ij}^{\mathrm{el}} + \dot{\varepsilon}_{ij}^{\mathrm{vi}} + \dot{\varepsilon}_{ij}^{\mathrm{pl}} \tag{4}$$

$\dot{\varepsilon}_{ij}$ denotes the total deviatoric strain rate tensor, while $\dot{\varepsilon}_{ij}^{\mathrm{el}}$, $\dot{\varepsilon}_{ij}^{\mathrm{vi}}$ and $\dot{\varepsilon}_{ij}^{\mathrm{pl}}$ represent the elastic, viscous and plastic strain rate components. A detailed discussion of this equation and all of its components is given by (Kaus et al., 2016), but here we will focus on the material parameters which impact the three components.

The elastic component $\dot{\varepsilon}_{ij}^{\mathrm{el}}$ is inverse proportional to the shear modulus G:

$$\dot{\varepsilon}_{ij}^{\mathrm{el}} = \frac{1}{2G}\frac{D\tau_{ij}}{Dt}, \tag{5}$$

where $D\tau_{ij}/Dt$ corresponds to the objective derivative of the stress tensor. For simplicity, we chose $G = 60$ GPa for all materials.

The viscous strain rate component $\dot{\varepsilon}_{ij}^{\mathrm{vi}}$ is subdivided into diffusion and dislocation creep (eq. 6):

$$\dot{\varepsilon}_{ij}^{\mathrm{vi}} = \dot{\varepsilon}_{ij}^{\mathrm{dif}} + \dot{\varepsilon}_{ij}^{\mathrm{dis}} = \frac{\tau_{ij}}{2}\left(\frac{1}{\eta_{\mathrm{dif}}} + \frac{1}{\eta_{\mathrm{dis}}}\right), \tag{6}$$

where η_{dif} and η_{dis} are defined as follows:

$$\eta_{\mathrm{dif}} = \frac{1}{2}(B_{\mathrm{dif}})^{-1}\mathrm{exp}\left(\frac{E_{\mathrm{dif}}}{RT}\right), \tag{7}$$

$$\eta_{\mathrm{dis}} = \frac{1}{2}(B_{\mathrm{dis}})^{-\frac{1}{n}}(\dot{\varepsilon}_{II}^{\mathrm{dis}})^{\frac{1}{n}-1}\mathrm{exp}\left(\frac{E_{\mathrm{dis}}}{nRT}\right), \tag{8}$$

where B is the creep constant, E the activation energy, $\dot{\varepsilon}_{II}^{\mathrm{dis}}$ the square root of the second invariant of the dislocation creep strain rate ($\dot{\varepsilon}_{II}^{\mathrm{dis}} = (\frac{1}{2}\dot{\varepsilon}_{ij}^{\mathrm{dis}}\dot{\varepsilon}_{ij}^{\mathrm{dis}})^{1/2}$), n the powerlaw exponent, R the universal gas constant and T the temperature.

The plastic component is characterized by the Drucker-Prager failure criterion (Drucker & Prager, 1952) which is a good approximation of Byerlee's law (Byerlee, 1978):

$$\tau_{II} \leq \sin(\phi)P + \cos(\phi)c_0 \tag{9}$$

τ_{II} is the square root of the second invariant of the stress tensor ($\tau_{II} = (\frac{1}{2}\tau_{ij}\tau_{ij})^{1/2}$), ϕ is the friction angle, P the pressure and c_0 the cohesion. Equation 9 describes how much stress can be accommodated with visco-elastic deformation.

In addition to the described rheology, we also employ lower and upper cut-offs to the effective viscosity of 10^{18} Pa s and 10^{25} Pa s respectively. The partitioning between the different rheological components cannot be solved analytically but requires local iterations in each node of the grid.

Table S1: List of Rheological parameters

unit	thickness (km)	reference density kg m^{-3}	prefactor (diff)	activation energy (diff) kJ/mol	activation volume (diff)	prefactor (disl)	activation energy (disl) kJ/mol	activation volume (disl)	n	Reference
Continental crust	0-40	2700	-	-	-	1.25×10^{-9}	123	0	3.2	(Tirel et al., 2008)
Upper mantle	100-660	3300	1.5×10^9	375	5×10^{-6}	1.1×10^5	530	8.5×10^{-6}	3.5	(Hirth & Kohlstedt, 2003)
Lower mantle	660-1000	3400	1.5×10^9	375	5×10^{-6}	1.1×10^5	530	8.5×10^{-6}	3.5	”
Continental lithosphere	40-100	2900	1.5×10^9	375	5×10^{-6}	1.1×10^5	530	15×10^{-6}	3.5	”
Cratonic lithosphere	100-200	3200 - 3400	1.5×10^9	375	9.5×10^{-6}	1.1×10^5	530	1.5×10^{-6}	10^6	”
Weak cratonic lithosphere	100-200	3200 - 3400	10^6	440	4×10^{-6}	90	260	11×10^{-6}	3.5	”
Slab	-	3300	1.5×10^9	375	9.5×10^{-6}	1.1×10^5	530	15×10^{-6}	3.5	”
Dense lower crust	30-70	3400-3550	10^6	335	4×10^{-6}	90	520	22×10^{-6}	3.5	”
Weak MLD	60-100	3300	10^6	440	4×10^{-6}	90	260	11×10^{-6}	3.5	”

Friction angle (ϕ) and cohesion (c_0) for all models are 30° and 10^6 Pa

Table S2: List of model parameters

Model	Hydration weakening	Weakening rate	Weak MLD	Dense lower crust	Reference craton density (ρ_{i}^{0}, kg m^{-3})	Destruction% after 100 Myr
M1	Yes	R1	No	No	3400	87
M2	Yes	R1	No	No	3300	66
M3	Yes	R1	No	No	3200	7
M4	Yes	R2	No	No	3400	87
M5	Yes	R2	No	No	3300	70
M6	Yes	R2	No	No	3200	7
M7	Yes	R3	No	No	3400	86
M8	Yes	R3	No	No	3300	47
M9	Yes	R3	No	No	3200	6
M10	No	-	No	No	3400	10
M11	No	-	No	No	3300	5
M12	No	-	No	No	3200	1
M13	No	-	No	Yes	3400	8
M14	No	-	No	Yes	3300	11
M15	No	-	No	Yes	3200	8
M16	No	-	Yes	No	3400	37
M17	No	-	Yes	No	3300	0
M18	No	-	Yes	No	3200	0

Additional Supporting Information (Files uploaded separately)

1. Captions for Movies S1

Movie S1. Animation showing the destruction of the NCC from model M2. Descriptions of different colors are given in Fig. 2.

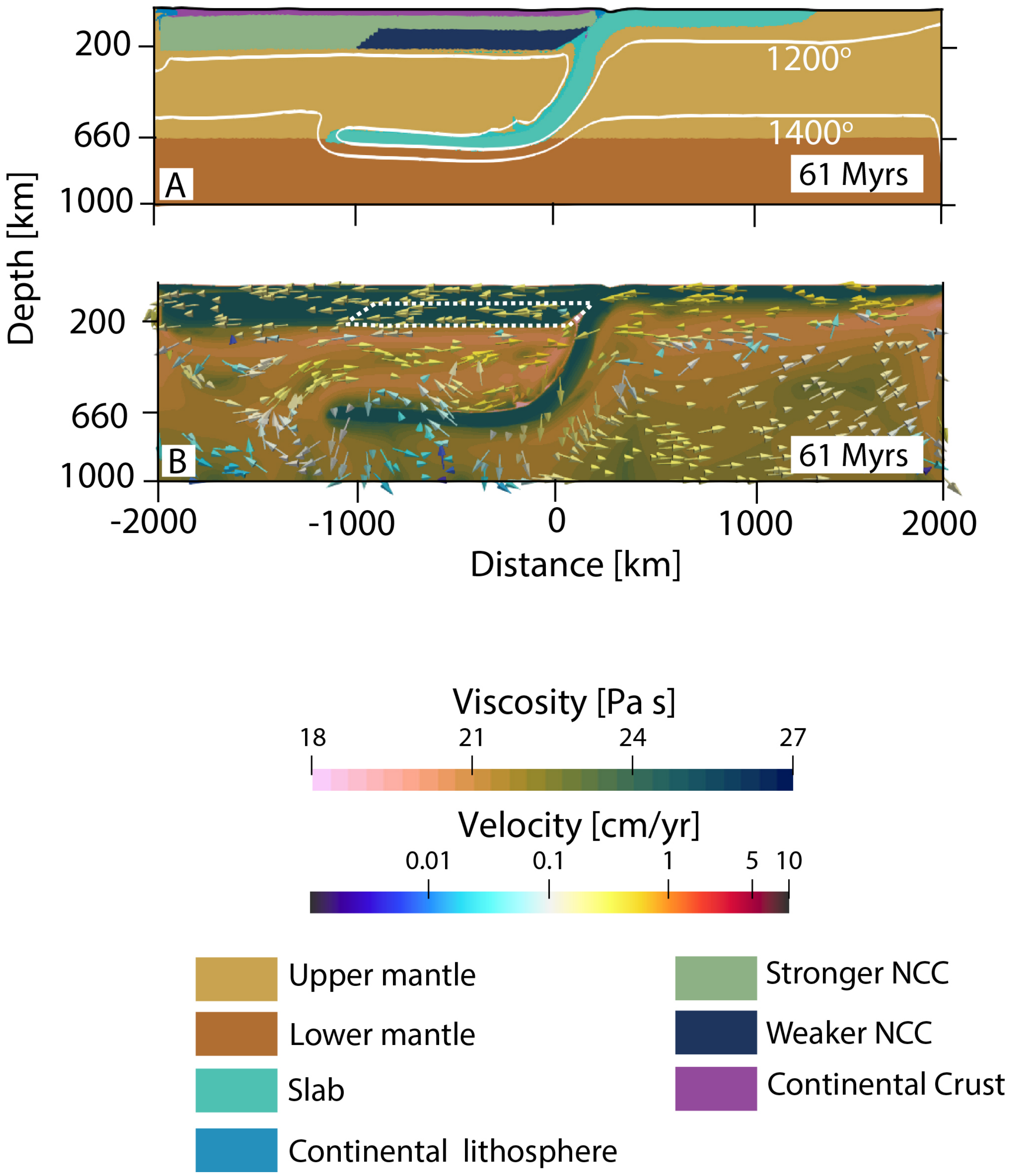

Figure S1. Snapshot of the NCC evolution from model M10 at 61 Myr. Background colors in A represent geological unit/phases which are indexed below. Dark blue region indicates the weak craton which is forming lithospheric drips. Solid white lines indicate isotherms of 1200 °C and 1400 °C. Background colors in B represent viscosity and the arrows represent mantle flow velocity. Viscosity and velocity scales are given below. White dashed line represents the craton, which is not destroyed in this model.

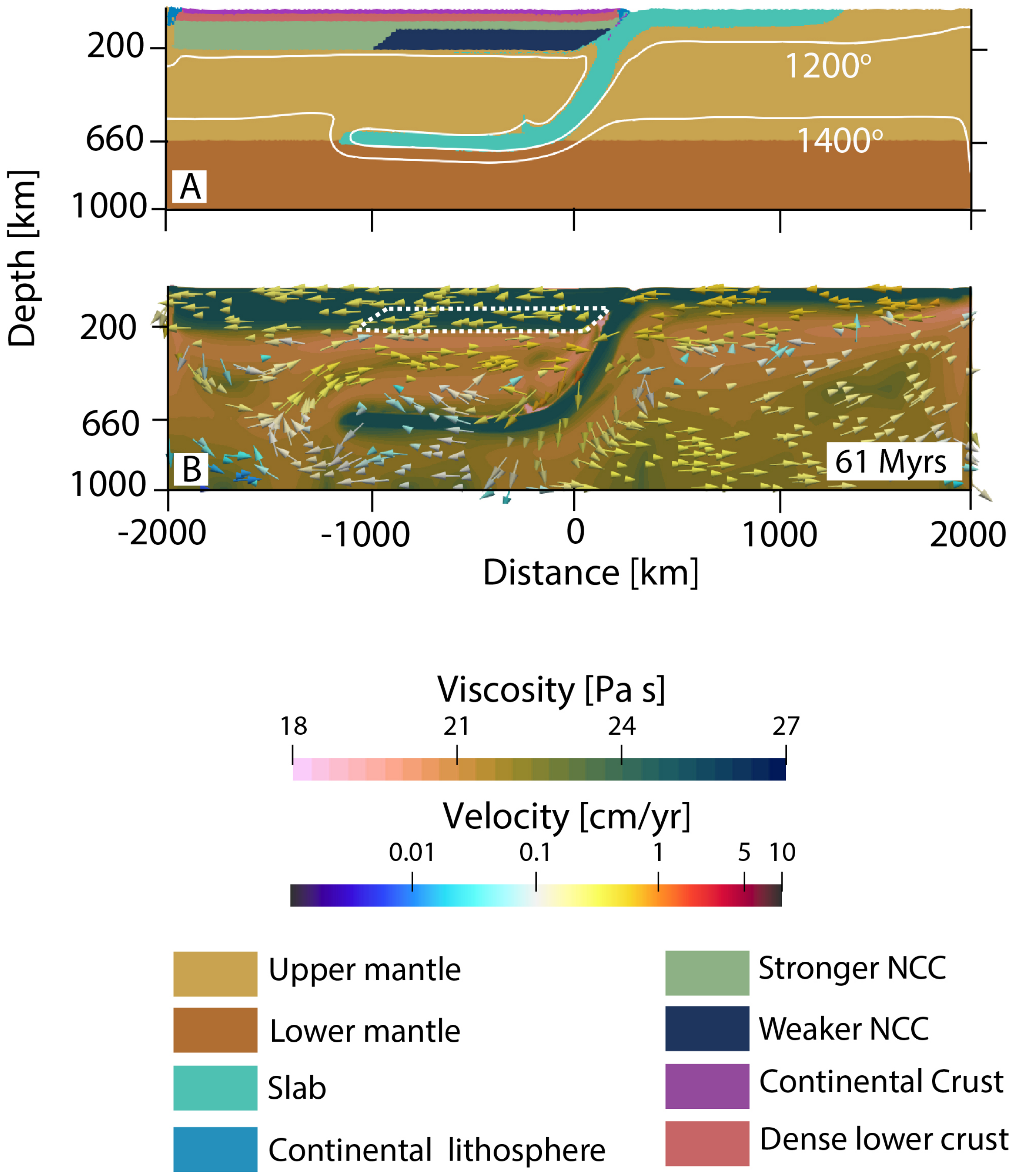

Figure S2. Snapshot of the NCC evolution in presence of a dense lower crust (pink colored region in A, model 13) at 61 Myr. Figure description is exactly same as the Fig. S1. No craton destruction observed in this model.

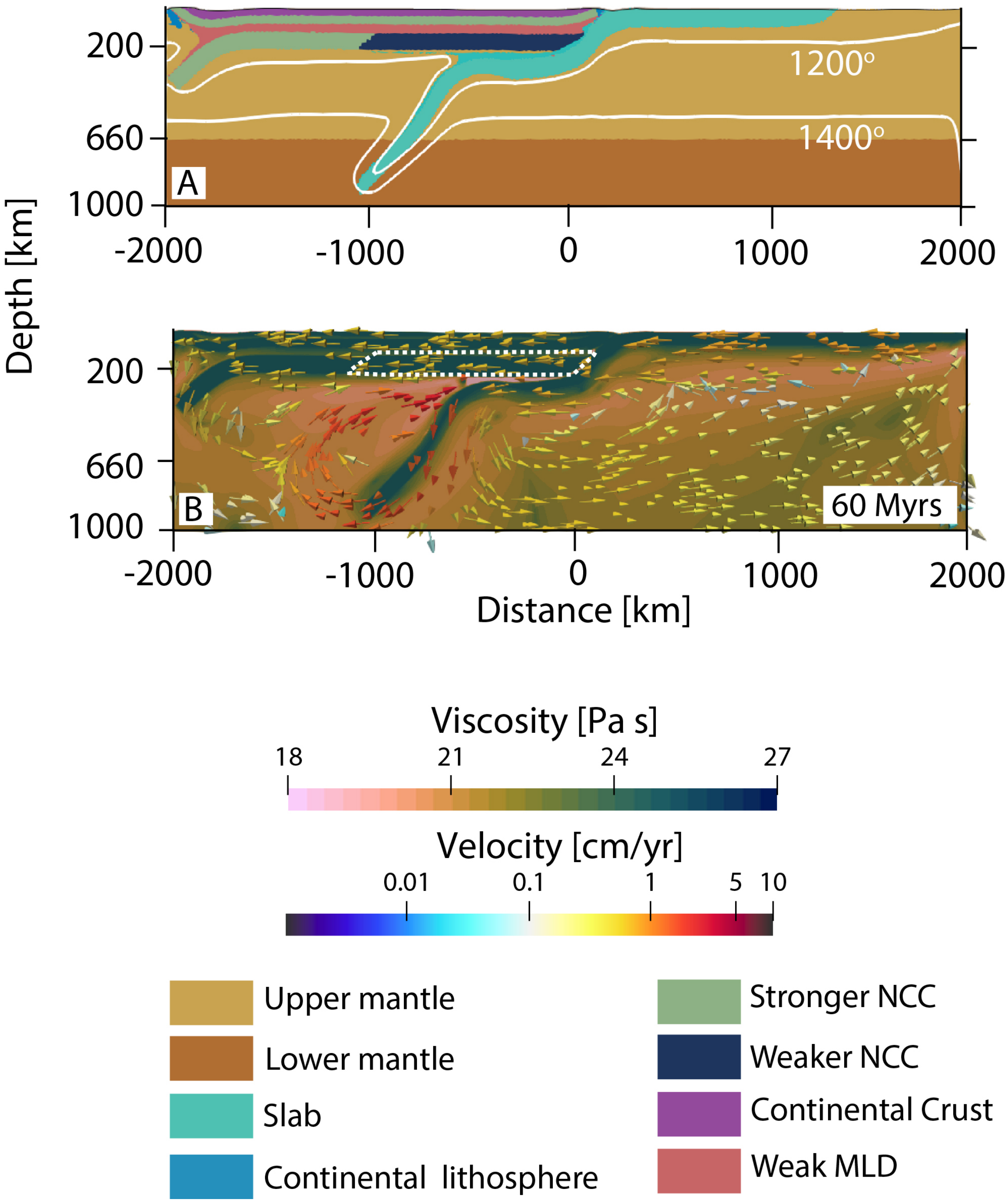

Figure S3. Snapshot of the NCC evolution in presence of a weak MLD (pink colored region in A, model 16) at 60 Myr. Figure description is exactly same as the Fig. S1. The craton starts delaminating from the western margin.

References

Byerlee, J. (1978). Friction of rocks. In *Rock friction and earthquake prediction* (pp. 615–626). Birkhäuser, Basel.

Drucker, D. C., & Prager, W. (1952). Soil mechanics and plastic analysis or limit design. *Quarterly of applied mathematics*, *10*(2), 157–165.

Duretz, T., May, D. A., Gerya, T., & Tackley, P. (2011). Discretization errors and free surface stabilization in the finite difference and marker-in-cell method for applied geodynamics: A numerical study. *Geochemistry, Geophysics, Geosystems*, *12*(7).

Harlow, F. H., & Welch, J. E. (1965). Numerical calculation of time-dependent viscous incompressible flow of fluid with free surface. *The physics of fluids*, *8*(12), 2182–2189.

Hirth, G., & Kohlstedt, D. (2003). Rheology of the upper mantle and the mantle wedge: A view from the experimentalists. *Geophysical monograph-american geophysical union*, *138*, 83–106.

Kaus, B. J., Mühlhaus, H., & May, D. A. (2010). A stabilization algorithm for geodynamic numerical simulations with a free surface. *Physics of the Earth and Planetary Interiors*, *181*(1-2), 12–20.

Kaus, B. J., Popov, A. A., Baumann, T., Pusok, A., Bauville, A., Fernandez, N., & Collignon, M. (2016). Forward and inverse modelling of lithospheric deformation on geological timescales. In *Proceedings of nic symposium.*

Tirel, C., Brun, J.-P., & Burov, E. (2008). Dynamics and structural development of metamorphic core complexes. *Journal of Geophysical Research: Solid Earth*, *113*(B4).